

Silicon Nanowire Field-Effect Transistors for Sensing Applications

Inauguraldissertation

zur
Erlangung der Würde eines Doktors der Philosophie
vorgelegt der
Philosophisch-Naturwissenschaftlichen Fakultät
der Universität Basel

von

Alexey Tarasov
aus Nowosibirsk



Basel, 2012

Genehmigt von der Philosophisch-Naturwissenschaftlichen Fakultät
auf Antrag von
Prof. Dr. C. Schönenberger
Prof. Dr. N. de Rooij
Prof. Dr. J. Linnros
PD Dr. M. Calame

Basel, den 16. Oktober 2012

Prof. Dr. Jörg Schibler
Dekan

Contents

Introduction	v
1 Basic terminology and device fabrication	1
1.1 Sensing principle and basic terminology	1
1.1.1 Basics of transistors	1
1.1.2 From transistors to ion sensors	4
1.2 Fabrication and device performance	5
1.2.1 The sample design	5
1.2.2 Fabrication process flow	5
1.2.3 Nanowire transistor characterisation in ambient	8
2 pH sensing	11
2.1 Measurement setup and conductance maps	11
2.2 Reaching ideal Nernstian pH response	15
2.3 pH response is independent of nanowire width	17
2.4 Real-time pH measurements	18
3 Noise measurements and detection limit	19
3.1 Introduction	19
3.2 Noise measurement setup	20
3.3 Results and discussion	20
3.4 Conclusions	25
4 Surface passivation and reference electrode	27
4.1 Introduction	27
4.2 The site-binding model	28
4.3 Experimental results and comparison with model	33
4.4 Conclusions	37
5 Understanding the electrolyte background for biochemical sensing	39
5.1 Introduction	39
5.2 Results and discussion	40
5.3 Conclusions	46

6	Additional investigations	49
6.1	Ionophores in a polymer membrane	49
6.2	Covalently bound ionophores	50
6.3	Sensing lectin-sugar interactions	53
	Conclusions and Outlook	57
	Appendix A: Device fabrication protocol 1	69
	Appendix B: Device fabrication protocol 2	79
	Appendix C: Protocol for covalent attachment of ionophores	83
	Appendix D: Surface modification protocol for lectin detection	85
	Publication List	87
	Curriculum Vitae	89
	Acknowledgements	91

Introduction

Sensing chemical and biological species is essential in many areas like diagnostics of diseases, screening and development of new drugs or environmental monitoring. All these fields experience a strong demand in transducers that convert specific (bio-)chemical processes into measurable signals. At the same time, the requirements put on such potential sensors are very high. The sensing devices have to be reliable, highly sensitive, sufficiently selective, multiplexed, and cost-effective. Combining all these features in one single sensing system has turned out to be a challenging task.

Existing techniques that use biochemical labels of the analytes are expensive, time-consuming and can influence the signals by modifying the target. Therefore, label-free methods that do not alter the target species are preferred. Optical methods like surface plasmon resonance (SPR) do not require labelling and have been successful in affinity studies. However, optical components are difficult to integrate on a large scale, and therefore a portable and low-cost sensor system, e.g. for personalized medicine, is beyond the means of SPR.

Ion-sensitive field-effect transistors (ISFETs) were invented in the 1970s and offer a promising set of features for integrating sensor and readout electronics on the same chip,¹ providing a portable and cost-effective solution. Such devices convert chemical reactions into electrical signals via electrostatic gating of the FET by adsorbed chemical or biological species. During the past decade, the ISFET concept has been applied to nanoscale devices such as carbon nanotubes,²⁻⁵ graphene⁶⁻⁹ or nanowires.¹⁰⁻¹² Due to their reliable and reproducible electrical properties, especially silicon nanowire FETs (Si NW FETs) have since covered a huge variety of applications, including pH sensing,^{11,13,14} label-free chemical^{11,15,16} and biosensing,^{11,12,17-20} flow velocity sensing,²¹ and detection of explosives.²² The considerable progress of nanoscale ISFETs has been driven by several factors. The key feature for biological applications is that the probe is comparable in size with the specimen, which is crucial for studies at the level of a single molecule or an organelle.^{23,24} More recently, the recording of potentials inside a living cell has been demonstrated using nanoscale FETs.^{25,26} The invasiveness of such measurements is strongly reduced thanks to the small sensor size. The reduced size also offers the possibility of a dense integration of differently

functionalized nanowires, which is useful for the multiplexed detection of analytes.^{11,17} Further noteworthy aspects of nanostructures are their high surface-to-volume ratios, that might enhance the sensitivity²⁷ and enable the detection of very diluted analytes^{12,17,28} as well as their small capacitances that reduce response times.²⁹

Even though many promising biosensing experiments with Si NW FETs have been performed, a detailed understanding of the basic sensing mechanism is still far from complete. Only little work has been done at a quantitative level. Also, many basic aspects have been so far neglected or only marginally addressed with sometimes inconsistent results, for example, evaluation of the signal-to-noise ratio, influence of the electrolyte background or implementation of reliable in-situ references to prevent misreadings.

The aim of this project has been to establish a robust and versatile sensing platform based on arrays of silicon nanowire field-effect transistors. We will present experimental results obtained during the past three years within this PhD thesis in the Nanoelectronics group of Prof. Christian Schönenberger at the University of Basel. A particular focus of this work has been put on the quantitative comparison of the experimental data with analytical models.

In Chapter 1, we will first present the necessary terminology of transistor physics and give a brief overview of the device fabrication process. In Chapter 2, we will present basic electrical measurements conducted in electrolyte environment and describe the pH response of nanowires. Chapter 3 will deal with noise measurements and will explore the detection limits set by the noise of the transistor. A way to realize a pH reference electrode by chemical surface passivation will be presented in Chapter 4. The experimental results will be accompanied by a quantitative theoretical description of the pH sensing mechanism. In Chapter 5, we will study the influence of the ionic background on the sensor response. We will show that existing models are not sufficient to describe our observations and present a new analytical model instead. Additional investigations going towards selective detection of ions and biomolecules will be discussed in Chapter 6. We will conclude this thesis with some final remarks and give an outlook.

1

Basic terminology and device fabrication

1.1 Sensing principle and basic terminology

1.1.1 Basics of transistors

The transistor (transfer resistor) is a semiconductor device used to switch or to amplify electrical signals, as they are transferred through it from input to output terminals.³⁰ First functional transistors were presented in 1947 by the team around W. Shockley at Bell Labs (Nobel Prize in Physics 1956). Since then, it has become the most important active electrical element of today's microelectronics. Each year, 10^{19} transistors are produced, or roughly a billion per person alive.³¹ There are two types of transistors: bipolar (resistance controlled by current) and field-effect (resistance controlled by voltage) transistors. The latter consume much less power and are therefore preferred for most of the applications. Here, we will present the very basics of transistor physics; the reader is referred to standard literature for a more detailed description, e.g.³²

The operating mechanism is illustrated using the example of the most frequently used transistor, the metal oxide semiconductor field-effect transistor (MOSFET). In Figure 1.1 a, a typical n-channel MOSFET is shown. The substrate is a p-type semiconductor, containing two highly n-doped regions called source and drain. A metal gate is placed on top of the semiconductor isolated by a metal oxide. The highly doped regions are isolated from

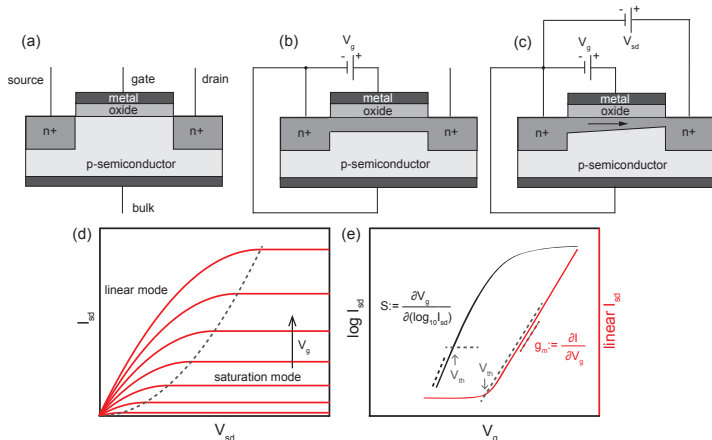


Figure 1.1: (a) Scheme of a typical n-channel MOSFET. The p-type semiconductor substrate (bulk) contains two highly n-doped regions (source and drain). A metal gate is placed on top of the semiconductor, isolated by an oxide. (b) Applying a positive voltage V_g between gate and source pulls electrons from the bulk to the semiconductor/oxide interface. An inversion channel is created. (c) If a positive voltage V_{sd} is applied between drain and source, electrons in the channel will move to the drain (arrow). The channel is narrowed by V_{sd} close to the drain. (d) Source-drain current I_{sd} vs. source-drain voltage V_{sd} for several gate voltages V_g . Dashed curve indicates the transition between linear and saturation mode. (e) Transfer curve $I_{sd}(V_g)$ on a semi-log (left vertical axis) and on a linear scale (right axis). The current is a linear function of V_g above the threshold voltage V_{th} (right curve). The slope is called the transconductance g_m . Below V_{th} , the current depends exponentially on the gate voltage. The exponential function is a straight line on a semi-log plot (left curve). Its reciprocal slope is known as the subthreshold swing S .

the substrate by p-n junctions. If a positive voltage is applied to the gate terminal, negative charge carriers are attracted to the semiconductor/oxide interface creating an inversion layer (Figure 1.1 b). Applying a voltage V_{sd} between the source and drain results in a current flow between both terminals (Figure 1.1 c). If no current flows at $V_{sd} = 0$, the transistor is called enhancement type or “normally-off”. In Figure 1.1 d, current-voltage characteristics are shown for several gate voltages. There are two different modes: the linear and the saturation mode. In the former, the inversion channel connects both n-doped regions; the transistor behaves like a simple resistor. The source-drain current I_{sd} through the channel is described by

$$I_{sd} = \mu C_{ox} \frac{W}{L} Q V_{sd} = \mu C_{ox} \frac{W}{L} (V_g - V_{th}) V_{sd} \quad (1.1)$$

with Q being the charge density in the channel, C_{ox} the capacitance of the gate oxide per area, W the channel width, L the channel length, V_{g} the gate voltage, V_{th} the threshold voltage and V_{sd} the source-drain voltage. Note that $I_{\text{sd}} = 0$ if $V_{\text{g}} \ll V_{\text{th}}$. This simple linear model is only valid for small source-drain voltages $V_{\text{sd}} \ll V_{\text{g}} - V_{\text{th}}$. The saturation mode occurs at higher V_{sd} . A positive source-drain voltage narrows the inversion channel close to the drain, as suggested by Figure 1.1 c. Above $V_{\text{sat}} = V_{\text{sd}} - V_{\text{th}}$, the channel is “pinched off” at the drain, and the electrons are forced to propagate through the substrate. The current is now nearly independent of V_{sd} (Figure 1.1 d).

A transfer characteristic is obtained when the source-drain current is measured as a function of the applied gate voltage (Figure 1.1 e). To switch the current on, a sufficiently large inversion channel is required, which is established above the threshold voltage V_{th} .

In the simple linear model discussed above, we assumed that the source-drain current is zero for gate voltages below the threshold voltage. However in a more accurate picture, a small source-drain current can flow due to the thermal activation of charge carriers as described by the Boltzmann statistics. One can show³³ that the subthreshold current is exponentially dependent on the gate voltage

$$I_{\text{sd}} \propto \exp\left(\frac{e}{kT} \cdot \frac{V_{\text{g}}}{1 + C_{\text{D}}/C_{\text{ox}}}\right) \quad (1.2)$$

with the depletion capacitance C_{D} , the gate oxide capacitance C_{ox} , the Boltzmann constant k , the elementary charge e and the absolute temperature T . The exponential function appears as a straight line on a semi-log scale (Figure 1.1 e), whose reciprocal slope defines an important parameter of a transistor, the subthreshold swing S :

$$S := \frac{\partial V_{\text{g}}}{\partial (\log_{10} I_{\text{sd}})} = \frac{kT}{e} \ln(10) \left(1 + \frac{C_{\text{D}}}{C_{\text{ox}}}\right) \quad (1.3)$$

The steeper the swing, the faster the FET can be switched. The minimum swing is given by $\ln(10)kT/e \approx 58.2$ mV/dec at 20°C.

The threshold voltage of a MOSFET V_{th} is defined as:

$$V_{\text{th}} = \phi_{\text{ms}} - \frac{Q_{\text{ox}} + Q_{\text{ss}} + Q_{\text{D}}}{C_{\text{ox}}} + 2\phi_{\text{B}} \quad (1.4)$$

where the first term $\phi_{\text{ms}} = \phi_{\text{m}} - \phi_{\text{s}}$ is the work function difference between the metal gate and the semiconductor, the second term is the sum of charges in the oxide Q_{ox} , at the oxide-semiconductor interface Q_{ss} and the silicon depletion charge Q_{D} . In the third term, twice the bulk potential $2\phi_{\text{B}}$ occurs to reach the onset of inversion.

1.1.2 From transistors to ion sensors

The ion-sensitive field-effect transistor (ISFET) was developed in the 1970s by Piet Bergveld and others.^{1,34} An ISFET is basically a MOSFET with the metal top-gate replaced by an electrolyte solution containing a reference electrode. The immersed electrode acts as a liquid gate, controlling the source-drain current of the ISFET. The gate dielectric is in contact with the liquid. The bare oxide surface is sensitive to pH, because the hydroxyl groups at the surface can take up or give away protons. The reactions with protons define the surface potential ψ_0 , which shifts if the proton concentration (pH) is changed. This surface potential shift modifies the threshold voltage. The Equation 1.4 now receives an additional (chemical) contribution and changes to:¹

$$V_{\text{th}} = E_{\text{ref}} - \phi_s - \psi_0 + \chi - \frac{Q_{\text{ox}} + Q_{\text{ss}} + Q_{\text{D}}}{C_{\text{ox}}} + 2\phi_{\text{B}} \quad (1.5)$$

with the constant potential of the reference electrode E_{ref} and the surface dipole potential χ of the solvent, which is a constant too. Note that the work function of the metal gate ϕ_{m} in the first term of Equation 1.4 is replaced by the electrode potential E_{ref} . The surface potential ψ_0 is the only term influenced by the pH. Quantitatively, the pH response is described by the combination of the Gouy-Chapman-Stern (GCS) theory with the site-binding model (SBM), which gives a useful relationship between the pH value of the bulk solution and the surface potential.^{14,35–39} The maximum possible shift of the surface potential due to a change in pH is given by the Nernst limit of $\ln(10)kT/e = 59.5 \text{ mV/pH}$ at 300 K, where k is the Boltzmann constant, T is the absolute temperature and e is the elementary charge. We will come back to the site-binding model in Chapter 4.

In principle, silicon nanowire ion-sensitive FETs presented in the following do the same measurement as the conventional ISFETs, i.e. they convert surface potential variations to changes in the channel conductance, but there are also differences. Nanowire ISFETs have a multigate device structure,¹⁴ and the nanowire itself acts as a conductive channel.⁴⁰ Also, we fabricate the devices using silicon-on-insulator wafers and operate them in accumulation rather than inversion. A sketch of the final device will be provided in the following section.

We will extensively use the shifts of the threshold voltage as the sensing signal later on. Thus, we will need a robust read-out method. In practice, the threshold voltage is often read out from the transfer curve on the linear scale, by taking the intercept of the linear fit with the axis $I_{\text{sd}} = 0$ (Figure 1.1 e, linear plot). This only works well if there is an extended region with constant transconductance $g_{\text{m}} = \partial I_{\text{sd}}/\partial V_{\text{g}}$. In nanoscale transistors, the

linear region can be rather short, especially if the contact resistances are relatively large.⁴⁰ The subthreshold regime is more reliable, because the region with constant subthreshold slope typically extends over several orders of magnitude. We then define V_{th} as a value of V_g at a constant I_{sd} in the subthreshold regime (horizontal dashed line in Figure 1.1e). The latter read-out method is used throughout this thesis, if not otherwise stated.

1.2 Fabrication and device performance

1.2.1 The sample design

To fabricate the silicon nanowire FETs, two different structures were used during this thesis. In the first part of this work, each sample consisted of four individual nanowires produced using standard UV lithography (Structure A, Figure 1.2). The dimensions of these wires were limited by the resolution of the technique. Typical widths ranged between 500 nm and $2\ \mu\text{m}$, the length was $10\ \mu\text{m}$, and the thickness was 60 – 80 nm. These single NWs were very useful at the beginning to demonstrate basic device functionality in ambient and liquid environment. In particular, first reliable and leakage-free operation in an electrolyte as well as reproducible pH sensing was shown using this structure.¹³ For practical applications however, nanowire arrays are preferable enabling e.g. differential measurements using multiple functionalization for the simultaneous detection of several analytes. Also, time-resolved correlation experiments would be possible with NW arrays. Having these goals in mind, a new design has been realized, containing 48 nanowires per chip, arranged in 4 clearly separated “pixels” (Structure B, Figure 1.3). First samples of this type were fabricated by UV lithography as before; later the NWs were produced in close cooperation with the Laboratory for Micro- and Nanofabrication at PSI Villigen, using a state-of-the-art e-beam writer. After several process optimization steps, including heavily-doped implanted contacts, RCA cleaning etc., a full wafer scale fabrication of highly reproducible nanowires with various widths (70 nm – $5\ \mu\text{m}$) was achieved. This allowed systematic size dependence studies and a high fabrication throughput in addition to the previously mentioned practical advantages of the nanowire arrays.

1.2.2 Fabrication process flow

At the beginning of this work, the samples (both single nanowires and NW arrays) were produced by UV lithography only (Protocol 1). The details of Protocol 1 can be found in the thesis by Oren Knopfmacher.⁴⁰ A copy of the protocol is included for convenience (Appendix A). Later, a combined

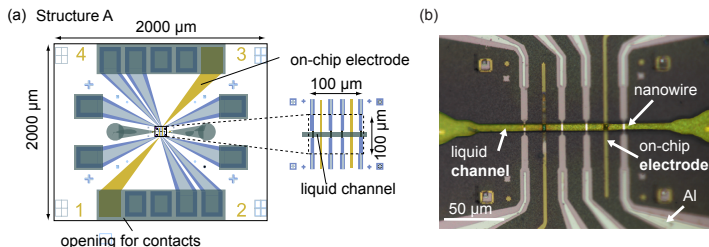


Figure 1.2: (a) Lithography mask layout of Structure A (4 single nanowires per sample), produced according to Protocol 1 (see Appendix A). (b) An optical image of a sample after lithography, including a liquid channel defined in a photoresist. The pictures are taken from.⁴⁰

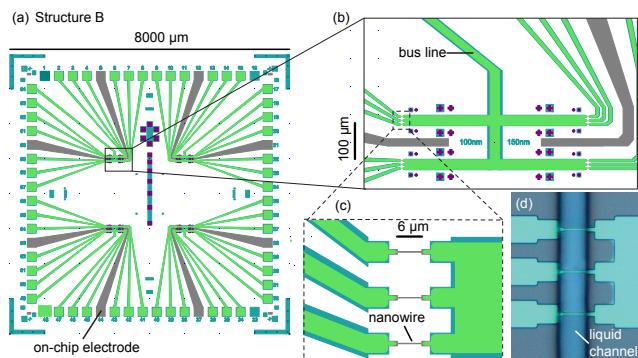


Figure 1.3: (a) Lithography mask layout of the nanowire array structure with 48 individually addressable nanowires, arranged in 4 so-called “pixels”. Each pixel (b) has 12 nanowires with a common bus line. (c) A close-up of the array with 100 nm wide NWs. (d) An optical image of three nanowires after lithography. The contact leads are sealed with a SU-8 photoresist, only a small area is exposed to the liquid (vertical liquid channel).

electron beam lithography (EBL) and UV lithography scheme was developed in cooperation with the PSI Villigen. While the detailed description of the various optimization steps and different sample generations will be extensively described in the PhD thesis by Kristine Bedner, we briefly introduce the most successful process flow so far (Protocol 2, for details see Appendix B). A commercial bonded silicon-on-insulator (SOI) wafer was used (SOITEC, France). First, a thin (~ 15 nm) thermal oxide was grown

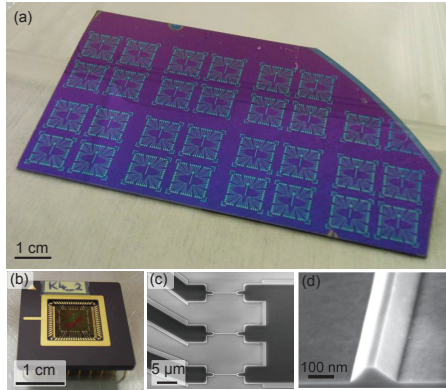


Figure 1.4: (a) An optical image of a wafer part after the lithography. (b) The chip after bonding into a chip carrier. (c) An SEM image of a nanowire array with contact regions. (d) An SEM image of a single nanowire. The trapezoidal shape is due to the anisotropic etching rates of Si in TMAH. Images by K. Bedner.

on the Si device layer. Then, the NW pattern was defined by EBL in a negative resist (AZ nLOF 2000) and transferred to the SiO₂ by reactive ion etching (CHF₃). The patterned oxide acted as a mask for the anisotropic wet chemical etching of the Si device layer using a solution of tetramethylammonium hydroxide (TMAH) and isopropanol at 45°C (9:1 volume ratio). The nominal dimensions of the NW were: width = 100–1000 nm, length = 6 μm, height = 80 nm). After the silicon etching, the source and drain areas were defined in PMMA by EBL. The resist was used as a mask for the ion implantation step (BF₂⁺, energy = 33 keV; dose = 2.3 · 10¹⁵ cm⁻², performed by Ion Beam Services, France) followed by thermal annealing in a forming gas (6 min at 950°C) to activate the dopants. The contact pads were formed by UV lithography, aluminum evaporation and annealing at 450°C. To reduce leakage currents in a liquid environment and to optimize the pH response, the samples were coated by a thin layer of a high-quality Al₂O₃ or HfO₂ (10–20 nm; atomic layer deposition (ALD) at 200–225°C, Savannah S100, Cambridge NanoTech). A standard RCA cleaning step was made prior to the high-temperature process, to optimize the silicon/oxide interface. The packaging for the operation in an electrolyte environment included a micrometer-sized liquid channel, lithographically shaped in a 2 μm thick photoresist (SU-8 2002, MicroChem), wire-bonding into a chip carrier and epoxy sealing of the contacts (Epotek 302-3M or 353ND, Epoxy Technology). Figure 1.4a shows a part of the 8 inch wafer after the lithog-

raphy. In Figure 1.4 b, one of the chips is shown after the wire bonding in the chip carrier. A SEM image of a NW array including the contact regions is depicted in part c, while the smallest nanowire is shown in part d. The trapezoidal shape is due to the anisotropic etching rates of Si in TMAH. The (111) plane is etched about 100 times slower than the (100) plane.¹² The NW side walls lie in the (111) plane at an angle of 54.7° relative to the (100) wafer surface.

1.2.3 Nanowire transistor characterisation in ambient

A sketch of the final device including the electrical scheme for test measurements under ambient conditions can be found in Figure 1.5 a (not to scale). The transistor properties of the nanowires were routinely tested after a thorough UV/ozone cleaning (10–30 min), showing high reproducibility and small hysteresis.⁴⁰ An example of a measurement in air is shown in Figure 1.5 b for three different nanowire top widths W_{top} . A small DC source-drain voltage $V_{\text{sd}} = 100$ mV is applied to the nanowire, and the source-drain current through the channel I_{sd} is measured as the back-gate voltage V_{bg} is swept. The contacts are heavily p-doped, and the nanowire transistors are operated in accumulation. When a negative voltage is applied to the back-gate, majority carriers (holes in the p-doped case) are accumulated in the nanowire, which acts as the conductive channel between source and drain. For more positive gate voltages, the nanowire is depleted, and no current can flow. For even more positive gate values, the channel should be inverted, i.e. populated by the minority carriers like in the n-MOSFET described before. However, no inversion current is observed in our case, because the contacts are highly p-doped. As a result, p-n junctions are formed between the contact regions and the inverted channel, preventing the electron transport through the nanowire. This is different to the thesis of Oren Knopfmacher, in which ambipolar (i.e. having both accumulation and inversion mode) nanowire FETs with low-doped contacts were used.⁴⁰ In the linear regime (left scale), the transconductance scales as expected with the nanowire width. No saturation is observed, because the contact resistance is relatively low. In the subthreshold range (right scale), no significant dependence of the subthreshold swing S on W_{top} is observed.

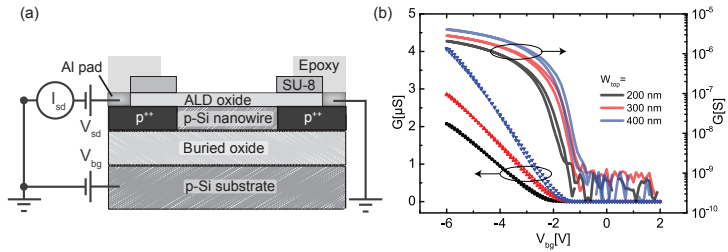


Figure 1.5: (a) A sketch of the final device and the measurement set-up used for the device characterisation in ambient (not to scale). The current through the channel I_{sd} is measured at a constant source-drain voltage V_{sd} as a function of the back-gate voltage V_{bg} applied to the Si substrate. (b) Nanowire channel conductance $G = I_{sd}/V_{sd}$ vs. V_{bg} for three different NW top widths W_{top} on linear and semi-log scale.

2

pH sensing

After successful fabrication, sealing and basic electrical testing of the samples under ambient conditions, as described in the previous chapter, we will now expose the active oxide interface of the nanowires to an electrolyte solution. We will first introduce the set-up used for most of the measurements in liquid presented throughout this thesis, and then explore the properties of the nanowires as pH sensors. Parts of this chapter have been published elsewhere^{13, 41, 42} or are submitted for publication.⁴³

2.1 Measurement setup and conductance maps

At the beginning of this thesis, single nanowire devices were measured using a lock-in technique at frequencies below 1 kHz. One goal of this project was to demonstrate the operation of nanowire arrays that have practical advantages over single NWs. The setup had to be changed to allow a fast readout of all nanowires. The technical details were discussed in Oren Knopfmacher's thesis.⁴⁰ The schematics of the measurement setup is shown for three NWs in Figure 2.1 a. In the new setup, a source-meter is used to apply the DC source-drain voltage V_{sd} and to measure the source-drain current through the NW channel I_{sd} . Using a switching box, all 48 NWs are automatically measured. The back-gate voltage V_{bg} is applied to the Si substrate, while the liquid gate voltage V_{lg} is applied to a Pt electrode, immersed in an aqueous solution (symbolized by the droplet). At the same time, the liquid potential

V_{ref} is measured by a calomel or a silver chloride reference electrode. In Figure 2.1 b, an optical image of a part of the sample can be seen.

The samples were cleaned by UV/ozone treatment (20 min) before the measurements. Then, a home-built liquid cell was placed on the chip and the first buffer solution with a well-defined pH value (Titrisol, Merck) was pumped through by a tubing pump (MCP, Ismatec). The samples were left for some time (30 – 120 min) in contact with the solution to stabilize the oxide/electrolyte interface. After that, a conductance map at the first pH value was measured by a source-meter as a function of both back-gate V_{bg} and the liquid potential V_{ref} (dual-gate approach^{13,44}) at constant source-drain voltage $V_{\text{sd}} = 100$ mV. Using a switching box, up to 48 NWs were measured in the same experiment to have some statistics and to study the size dependence. As soon as such conductance map was obtained, the pH buffer solution was exchanged using a low-pressure valve selector (VICI Cheminert, Valco Instruments Co. Inc.) and a pump. Again, a map was measured after some stabilization time (10 – 30 min) at a new pH value. All devices were automatically controlled by a self-made LabView program.

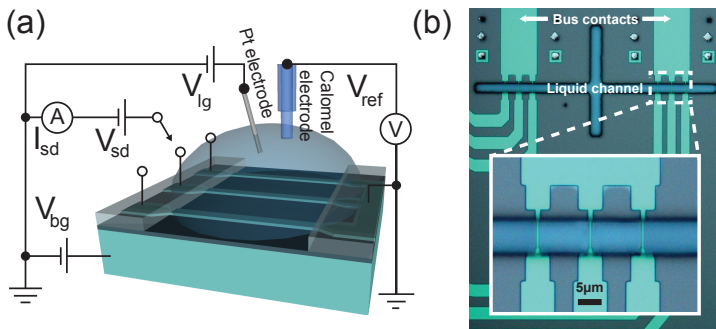


Figure 2.1: (a) Schematics of the measurement setup, shown for three nanowires (NWs). A source meter is used to apply the source-drain voltage V_{sd} and to measure the source-drain current I_{sd} . Using a switching box, up to 48 NWs are automatically measured. The back-gate voltage V_{bg} is applied to the Si substrate, while the liquid gate voltage V_{lg} is applied to an immersed Pt electrode. At the same time, the liquid potential V_{ref} is measured by a calomel reference electrode. (b) Optical image of a part of the sample, showing six nanowires and contact leads (vertical lines). Three NWs share a common bus line to save contacts. A liquid channel is defined in a SU-8 photoresist to minimize leakage currents (cross-like structure). In total, 48 NW FETs with 8 different widths (100 nm – 1 μ m) are defined on one chip. Inset: a close-up shows three nanowires (thin vertical lines, 400 nm nominal NW width) and the horizontal liquid channel.

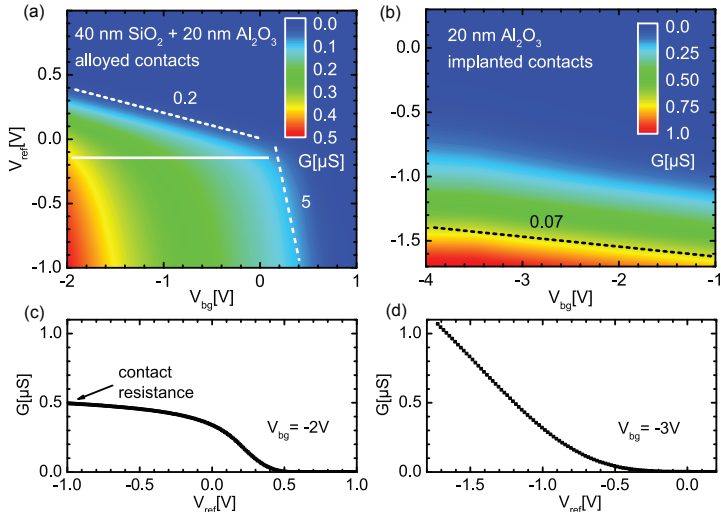


Figure 2.2: (a) Contour plot of the conductance G vs. the back-gate voltage V_{bg} and the liquid potential V_{ref} at pH 7. The data is from a sample with alloyed contacts (700 nm wide NW), therefore two regimes occur: above and below the solid line. In the lower regime, the contact resistance dominates. Whereas in the upper case, the contact resistance can be neglected, and the nanowire resistance dominates. This results in different gate coupling capacitance ratios between the back- and the liquid top gate C_{bg}/C_{lg} (dashed lines and numbers). Here, the top gate oxide consists of two layers: thermal SiO_2 and ALD-grown Al_2O_3 . (b) Data from a 100 nm wide NW with highly-doped implanted contacts. No contact-dominated regime is visible any more. The capacitance ratio $C_{bg}/C_{lg} \approx 0.07$ is smaller than in (a), because of the thinner top oxide and hence larger top oxide capacitance $C_{TOP} \approx C_{lg}$. (c) Transfer curve $G(V_{ref})$ corresponds to a vertical cut through the map (a) at a fixed $V_{bg} = -2\text{V}$. The total conductance G saturates at $V_{ref} < 0$ due to the large resistance of alloyed contacts ($\sim 2\text{M}\Omega$). (d) A cut through the map (b) at $V_{bg} = -3\text{V}$ does not show any saturation in the measured range. The contact resistance is much lower than in (c).

In the following, we will show and discuss several conductance maps, obtained with Al_2O_3 (Figure 2.2) and HfO_2 -coated samples (Figure 2.3). All maps were measured in a buffer solution at pH 7. In Figure 2.2a, a contour plot of the conductance $G(V_{bg}, V_{ref})$ for a nanowire with low-doped contacts (evaporated and alloyed aluminum) is shown, which was fabricated according to Protocol 1 (see Appendix A). In this case, the nanowire was covered by 40 nm thermal SiO_2 and 20 nm ALD-grown Al_2O_3 . The solid horizontal line marks the border between two different regimes, which differ in their relative coupling to the two gates.^{13,45} The dashed lines and numbers indicate the slopes of the equal conductance lines in the two different

regions. These slopes are determined by the ratio of the gate coupling capacitances $C_{\text{bg}}/C_{\text{lg}}$, where C_{bg} is the buried oxide capacitance and C_{lg} is a series connection of the total top oxide capacitance C_{TOX} and the double-layer capacitance C_{dl} . Because $C_{\text{dl}} \gg C_{\text{TOX}}$,^{1,41} we conclude $C_{\text{lg}} \approx C_{\text{TOX}}$. Note that in Figure 2.2 a, C_{TOX} is a series connection of both SiO_2 and Al_2O_3 layer capacitances. To understand the origin of the two different regimes, one has to see that the NW-FET resistance $R = 1/G$ is composed of two resistances in series. The intrinsic resistance R_{NW} and the contact resistance R_c . Due to the confinement of the liquid channel to the NW, R_c is only weakly affected by the liquid gate (small C_{lg}). Hence, if R_c dominates R , $C_{\text{bg}}/C_{\text{lg}}$ is large, which corresponds to the lower regime. In contrast, if R_c can be neglected, R is determined by R_{NW} , which on its own is more strongly capacitively coupled to the liquid than to the back-gate. We refer to the two regimes as contact and NW dominated.

We know now that the steep slope in the lower region is due to the gating of the contact leads by the back-gate.^{13,40} This issue disappears if highly-doped contacts are used that are barely influenced by the gates. In Figure 2.2 b, a nanowire coated with 20 nm Al_2O_3 and implanted contacts is shown (Protocol 2, see Appendix B). No contact-dominated region is visible any more. To illustrate the contact resistance issue more clearly, vertical cuts through the contour plots at a constant V_{bg} were made. Such cuts (or transfer curves $G(V_{\text{ref}})$) are plotted in Figure 2.2 c and d. In the case of the low-doped contacts (c), the transfer curve saturates for $V_{\text{ref}} < 0$ V because of the contact resistance. In contrast, an extended linear region is observed in the highly-doped case (d).

Similar conductance maps for HfO_2 -coated samples are presented in Figure 2.3 a (10 nm thick oxide) and b (20 nm). As expected, doubling the thickness results in a doubling of the capacitance ratio (dashed lines and numbers). The ratio is lower than in the case of Al_2O_3 due to the higher relative permittivity ϵ_r of HfO_2 . In fact, ϵ_r of the top oxides can be estimated based on the capacitance ratios via

$$\frac{C_{\text{bg}}}{C_{\text{lg}}} = \frac{\epsilon_{r,\text{BOX}} t_{\text{TOX}}}{\epsilon_{r,\text{TOX}} t_{\text{BOX}}} \quad (2.1)$$

with $\epsilon_{r,\text{BOX}} = 3.9$ being the relative permittivity of the buried SiO_2 , its thickness $t_{\text{BOX}} = 145$ nm, the (known) thickness of the top oxide t_{TOX} and the (unknown) $\epsilon_{r,\text{TOX}}$. From Figure 2.2 b we estimate $\epsilon_{r,\text{TOX}} \approx 7 - 9$ for Al_2O_3 , and $\epsilon_{r,\text{TOX}} \approx 20 - 25$ for HfO_2 (from Figure 2.3). These relative permittivities are consistent with previously reported values (9 for Al_2O_3 and 25 for HfO_2).⁴⁶ Further aspects of the gate oxide characterization will be covered in the PhD thesis of Kristine Bedner.

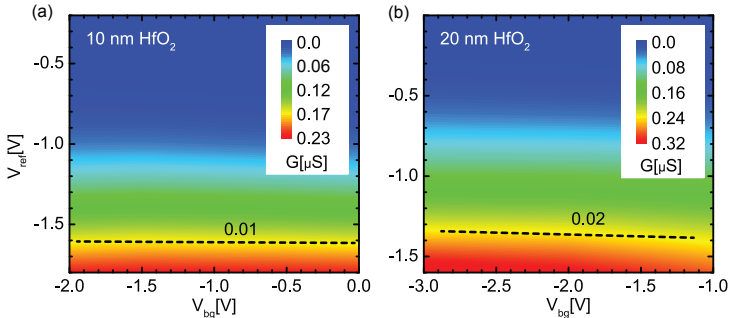


Figure 2.3: Conductance G maps vs. both the liquid potential V_{ref} and the back-gate voltage V_{bg} for a 100 nm wide NW with 10 nm (a) and 20 nm HfO_2 (b) as top oxide, measured at pH = 7. The dashed lines and numbers represent the gate capacitance ratio between the back- and the liquid gate $C_{\text{bg}}/C_{\text{lg}}$. The ratio is higher in (b) because of the thicker top oxide.

2.2 Reaching ideal Nernstian pH response

To characterize the transistor response of the nanowires in liquid, a sweep of the liquid potential is made at a fixed V_{bg} and V_{sd} . In 2.4 a, such up and down liquid gate sweeps are shown for two different nanowires on both linear and semi-log scale. All curves align very well on top of each other, demonstrating a negligible hysteresis (< 10 mV) and highly reproducible device properties. Because of the highly-doped implanted contacts, an extended linear range with nearly constant transconductance is observed, in contrast to our previous protocol with alloyed contacts.^{13,40,41,45} The subthreshold swing is around 100 mV/dec, which is a good value, compared to the ideal slope of ~ 60 mV/dec. To test the pH response of the nanowire, we exchange the buffer solution several times and measure the transfer curve again for each pH value. Typical results from a HfO_2 -coated nanowire are depicted in Figure 2.4 b. The curve shifts to more positive V_{ref} values as the pH value of the solution increases. The same data is plotted in Figure 2.5 b to compare with an Al_2O_3 -coated nanowire shown in Figure 2.5 a. To quantify the pH response, we define the threshold voltage V_{th} of the FET as the liquid potential value at a constant conductance $G = 10^{-8}$ S in the subthreshold regime (see arrow in Figure 2.5 a). This G value is chosen because it is deep inside the subthreshold regime but still well above the noise. Other values would also meet these requirements without affecting the readout quality of the threshold shifts. The threshold voltage is then plotted as a function of the solution pH value for both oxides in the insets of Figure 2.5 (squares).

The pH response is extracted from the linear fits to these data points (solid lines), and is very close to the theoretical maximum of ~ 58.2 mV/pH at 20°C (Nernst limit) in both cases. This result is associated with the high quality of the ALD oxide layers that provide a large number of active proton-binding surface OH groups, in contrast to the most widely used SiO_2 . A detailed quantitative explanation within the site-binding model will follow in Chapter 4.

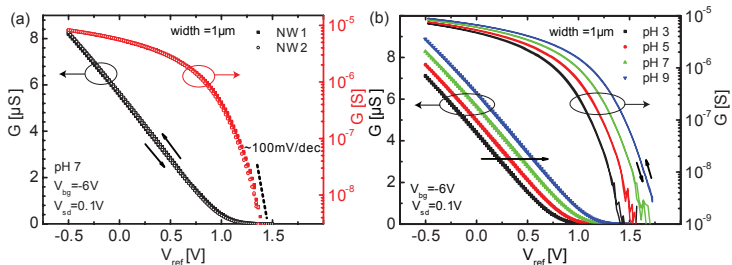


Figure 2.4: (a) Conductance G vs. the liquid potential V_{ref} (transfer curves) for two different HfO_2 -coated nanowires of the same size, on linear (left) and semilog (right) scale. Both up and down gate sweeps are shown (arrows). All curves align very well on top of each other, showing high reproducibility and negligible hysteresis. (b) Transfer curves of one nanowire at different pH values. Increasing the pH shifts the curve to more positive V_{ref} values.

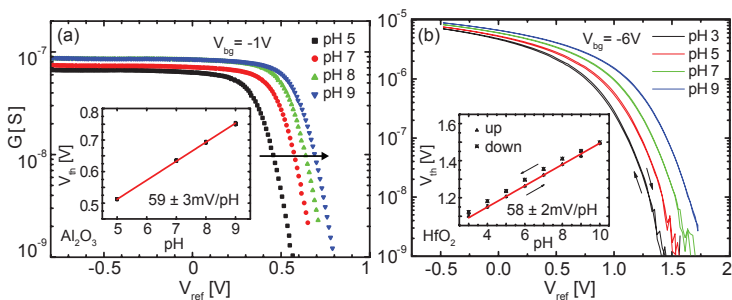


Figure 2.5: Transfer characteristics of a Al_2O_3 -coated NW (a) and a HfO_2 -coated one (b) at different pH values. Inserts: threshold voltage V_{th} as a function of pH. We define V_{th} as the liquid potential value at a constant conductance $G = 10^{-8}$ S in the subthreshold regime (along the arrow in (a)). Solid lines are linear fits of $V_{\text{th}}(\text{pH})$. A nearly ideal Nernstian response of ~ 58 mV/pH at 20°C is achieved with both oxides.

2.3 pH response is independent of nanowire width

Here, we study the pH response as a function of the nanowire width ranging from 100 nm to 1 μm (Figure 2.6). A manuscript covering this topic has been submitted.⁴³ The size dependence will be extensively discussed in the PhD thesis by Kristine Bedner. In part a of the Figure 2.6, a SEM image of a nanowire is shown. Along the solid lines, a schematic cross-section of a nanowire is made (b), where W_{top} is the top width of the trapezoidal nanowire. In c, the pH response is plotted against the nanowire top width W_{top} for both oxides. All NWs show a nearly ideal Nernstian behavior of $\sim 60 \text{ mV/pH}$ at 300 K (dashed line), independent of the NW width and the gate oxide type. The pH response is defined as before, a threshold voltage vs. pH plot is shown for the three narrowest nanowire widths in the inset. To our knowledge, this is the first systematic study reporting a clear absence of any size dependence on pH sensing properties of NWs. The observed ideal pH response confirms recent results showing that ALD-grown Al_2O_3 ⁴¹ and HfO_2 ⁴⁷ are excellent pH sensing interfaces, due to the high density of active surface groups that buffer the pH changes in the bulk solution. Within the site-binding model,¹ this oxide property is called the surface buffer capacity. As long as the oxide/electrolyte interface of the nanowire surface provides a large surface buffer capacity for protons, no size dependence is expected. Our observation is in contrast to the works by Ref.^{27,48} We will describe the site-binding model in much more detail in Chapter 4.

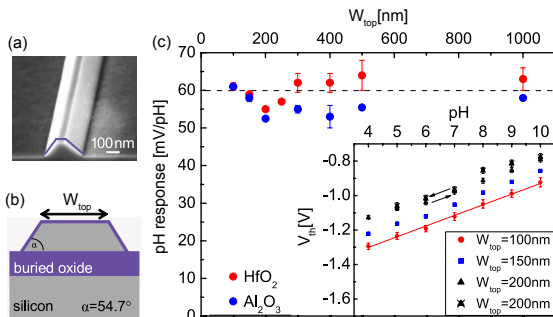


Figure 2.6: (a) SEM image of a nanowire. (b) Schematic cross-section of a nanowire along the lines in (a). The top width W_{top} varies between 100 and 1000 nm. (c) The pH response vs. W_{top} for both interface oxides. Inset: threshold voltage V_{th} vs. pH shown for three narrowest nanowires. A linear behavior is observed over the whole range. The pH response is defined by the slope of the best fit line. Measurements for increasing (triangles) and decreasing pH (triangles with crosses) lie almost on top of each other (arrows). Images by K. Bedner.

2.4 Real-time pH measurements

In addition to recording transfer curves, one can also choose a fixed working point of the NW FET, and measure the source-drain current I_{sd} as a function of time t . This measurement technique is particularly interesting for biosensing, for example to quantify the affinities and kinetics of protein interactions.⁴⁹ Both measurement techniques are compared for the same nanowire in Figure 2.7. First, the transfer curves are measured to characterize the device, showing a near-Nernstian pH response as discussed before (Figure 2.7 a). Note that this time the source-drain current I_{sd} is plotted against V_{ref} , rather than the conductance G . This is done to extract the maximum transconductance $g_m = \delta I_{sd} / \delta V_{ref}$ from the first derivatives of the presented curves. The transconductance variations between different curves are very small. An average value of $|g_m| \approx 5.65 \pm 0.05 \cdot 10^{-7}$ A/V (dashed line) is then taken to convert the measured real-time pH response $I_{sd}(t)$ to the threshold voltage shift $\Delta V_{th} = \Delta I_{sd} / g_m$ (Figure 2.7 b). This conversion results in a Nernstian response close to 60 mV/pH, very similar to the values extracted from the shifts of the transfer curves. The working point ($V_{ref} = 0.4$ V) was chosen to be in the linear regime, i.e. where the transconductance is nearly constant. The response time (jump between two adjacent pH values) is in the range of seconds and is given by the liquid exchange rate. Increasing the exchange rate leads to response times < 200 ms.

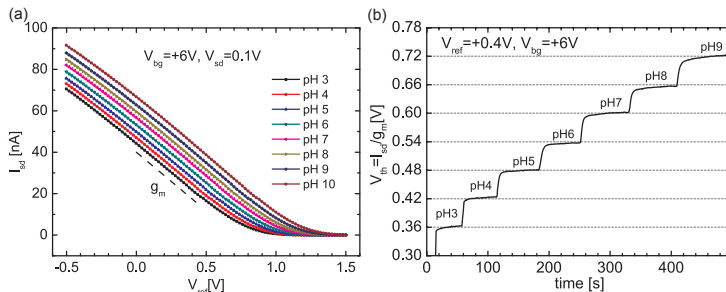


Figure 2.7: (a) Transfer curves of a $1 \mu\text{m}$ wide NW at different pH values. The transconductance $g_m = \delta I_{sd} / \delta V_{ref}$ is obtained by taking the first derivative of the $I_{sd}(V_{ref})$ curves. (b) Real-time sensor response to the changes in pH. The measured source-drain current I_{sd} is converted to a threshold voltage shift ΔV_{th} , using the transconductance value from (a). The distance between two horizontal grid lines is 60 mV, showing Nernstian response of the sensor.

3

Noise measurements and detection limit

In the previous chapter, we demonstrated highly reproducible device performance in liquid environment, combined with a full Nernstian pH response. In the following, we will measure the low-frequency $1/f$ noise and evaluate the detection limit of our pH sensors. Parts of this chapter have been published elsewhere.⁴⁵

3.1 Introduction

Apart from the pH response, the evaluation of noise is also an important issue, as it ultimately defines the detection limit of a sensor. Recently, intense attempts have been made to understand the factors determining the signal-to-noise ratio,^{8, 50–54} however with inconsistent conclusions about the optimal regime for sensing. Studies on carbon nanotube FETs⁵⁰ and on nanowire FETs⁵¹ claimed that the signal-to-noise ratio (SNR) increases in the subthreshold regime, which would therefore be the preferred regime for high sensitivity. In contrast, Rajan and co-workers⁵⁴ argued that the SNR in silicon nanowires is optimized in the linear regime around the maximum transconductance. Here, we resolve this disagreement by measuring the $1/f$ noise over the full operating range of the FET and evaluating the detection limit set by the noise of the transistor.

3.2 Noise measurement setup

Silicon NW-FETs were produced according to Protocol 1 (Appendix A). The dimensions of the presented nanowires were: length \times width \times height = $10\ \mu\text{m} \times 700\ \text{nm} \times 80\ \text{nm}$ (Figure 3.1 a). A special set-up was used for the noise measurements, the schematics is provided in Figure 3.1 b. The NW FETs were operated at low source-drain DC voltages $V_{\text{sd}} = 10 - 100\ \text{mV}$ in the linear regime. The source-drain current I_{sd} through the NW was measured by a current-voltage converter with a variable gain ($10^5 - 10^9\ \text{V/A}$). The conductance G of the NW-FET is then obtained as the ratio $G = I_{\text{sd}}/V_{\text{sd}}$ while varying both the back-gate V_{bg} and liquid gate voltage V_{lg} . This yields a two-dimensional (2D) conductance map, as introduced in Chapter 2 (see Figure 3.1 c). The vertical axis V_{ref} is the potential of the liquid, as measured by a calomel reference electrode. The equivalent voltage noise power spectral density S_V (see e. g. ⁵⁵) was determined along the solid white lines through a fast Fourier transform of the time dependent fluctuations of I_{sd} .

3.3 Results and discussion

In this section, we present the results from samples with low-doped alloyed contacts. Therefore, the contribution of the contact resistance to the conductance and the noise properties has to be taken into account. We will see that using the dual-gate approach, the FET can be tuned to a region where the additional noise contribution from the contact regions is minimized. The situation is explained with the help of the conductance map in Figure 3.1 c. This map displays two different regimes, above and below the white dashed line at about $V_{\text{ref}} = +0.4\ \text{V}$. As already discussed in the previous chapter, the regime above the line is dominated by the intrinsic nanowire resistance, whereas the lower regime is dominated by the contact resistance. Short lines and numbers indicate the ratio of the gate coupling capacitances at a constant conductance value. The noise is measured along the colored solid lines.

Figure 3.2 shows the frequency dependence of the noise power $S_V(f)$ of the NW for different resistance values, measured in air (a) and in a buffer solution with pH 7 (b). The corresponding thermal background noise, recorded at zero bias, has been subtracted from the data. An example is shown by (Δ). $S_V(f)$ has a clear $1/f$ dependence (dashed lines), and its amplitude is proportional to V_{sd}^2 (inset), as expected for $1/f$ noise.⁵⁵ Such a behavior can phenomenologically be described by Hooge's law^{55,56}

$$S_V(f) = V_{\text{sd}}^2 \frac{\alpha}{Nf} \quad (3.1)$$

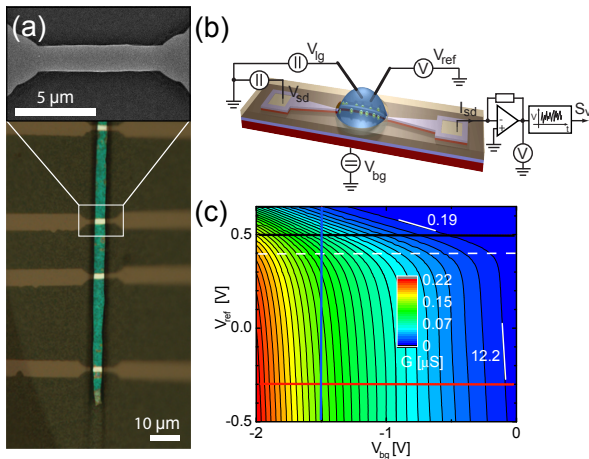


Figure 3.1: (a) Optical image of a sample with four nanowires (NWs) (horizontal) and an enlarged SEM image of one of the NWs. The (vertical) liquid channel is the only part of the sample which is not covered with photoresist. (b) A schematic representation of the setup used for the measurements in liquid. There are two gates, a back-gate and a liquid-gate with applied gate voltages V_{bg} and V_{lg} . The liquid potential is measured by a calomel reference electrode and denoted as V_{ref} . The NW-FETs are characterized by their conductance map $G(V_{bg}, V_{ref})$, shown in (c), and by the noise obtained from the temporal dependence of the source-drain current I_{sd} using fast Fourier transform. In (c) the horizontal dashed line marks the border between two regimes, the nanowire (upper) and contact (lower) dominated regime. Noise measurements were conducted along the three solid colored lines. Short solid lines and numbers represent the slopes of the equiconductance lines.

The material dependent parameter α accounts for scattering effects and the constant N denotes the number of fluctuators in the system.

In Figure 3.3, the normalized noise amplitude S_V/V_{sd}^2 at 10 Hz is depicted as a function of R . The noise in the system increases dramatically (indicated by dashed lines) above a certain threshold resistance value. The position of this threshold (arrows) and the steepness of the rise depends on whether the NW is gated by the liquid or the back-gate. In air (\blacktriangledown), where V_{bg} is the only applied gate voltage, the noise starts to increase at roughly 30 M Ω . A similar behavior is observed in liquid in the contact-dominated regime, i.e. for $V_{ref} = -0.3$ V (\blacksquare). In contrast, within the NW-dominated regime (\bullet), the noise increases steeper, starting already at about 10 M Ω . For R smaller than the respective thresholds, the noise level is approximately constant. The apparent superimposed structure observed in this range is wire specific. Different NW-FETs, while confirming the general dependence, typically dis-

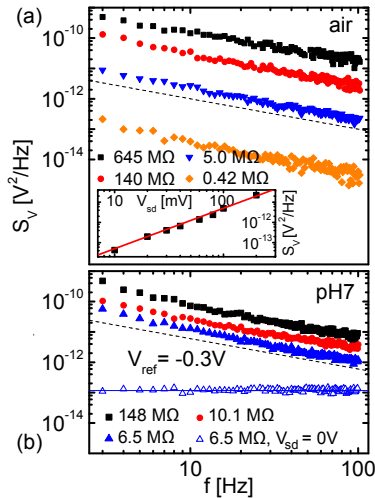


Figure 3.2: The noise power spectral density of the voltage fluctuations S_V obtained for a source-drain bias voltage of $V_{sd} = 90$ mV for different resistances of a NW measured (a) in air and (b) in a buffer solution (Titrisol pH 7, Merck). The dashed lines indicate a $1/f$ slope. The open symbols in (b) represent the thermal noise of the NW at $V_{sd} = 0$ V (Δ). The calculated thermal noise of a 6.5 M Ω resistor at 300 K is shown for comparison (horizontal line). Inset: S_V as a function of V_{sd} at 7 Hz, measured in air (logarithmic scale). The solid line indicates a power law with exponent two.

play a different fine structure. The thresholds of $10 - 30$ M Ω correspond to the transition from the linear to the subthreshold regime of the FETs. Note that the linear regime is limited by the resistance of the contact leads.

The physical signal in FET sensors is the shift δV_{th} of the threshold voltage V_{th} caused by a chemical change on the sensing surface. It is obtained from the measured conductance change ΔG and the transconductance $g = G' = dG(V_g)/dV_g$, characteristic for a given FET, as $\delta V_{th} = \Delta G/g$. This equation can be used to determine the true figure of merit which is the equivalent noise power of the threshold voltage δV_{th} given by

$$\delta V_{th} = \frac{\sqrt{S_V/V_{sd}^2(f)}}{g/G} = \frac{\sqrt{S_V/V_{sd}^2(f)}}{(\ln G)'} \quad (3.2)$$

Here, we have made use of the relation $\delta G/G = \sqrt{S_V}/V_{sd}$.

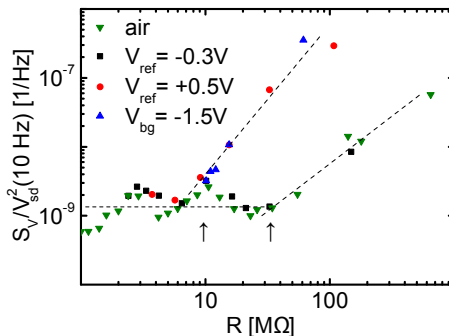


Figure 3.3: S_V divided by the squared source-drain voltage V_{sd}^2 as a function of R at 10 Hz, measured in air and in buffer solution (logarithmic scale). Dashed lines are guides to the eye. Arrows indicate the transition between different regimes.

In Figure 3.4 a we show δV_{th} when the controlling gate is V_{bg} for data measured in air (\blacktriangledown) together with the data acquired in buffer solution at $V_{ref} = -0.3$ V (\blacksquare). Both curves show a very similar behavior. Since we know that the liquid data obtained at $V_{ref} = -0.3$ V is contact dominated, we conclude that the measurement in air is also contact dominated.

In Figure 3.4 b we summarize δV_{th} for measurements done in an electrolyte. To obtain δV_{th} , we consistently use V_{bg} as the controlling gate for all three data sets in this figure. Interestingly, in the NW-dominated regime (\bullet) δV_{th} is much smaller than in the contact-dominated regime (\blacksquare). The difference can amount to almost two orders of magnitude. Although the voltage noise values S_V are not much different in the two regimes (Figure 3.3), the sensitivities in the true measurement quantity greatly differ. This shows that the transconductance values, and therefore the gate-coupling to the liquid, are crucial factors determining the ultimate sensitivity. We also stress that δV_{th} can be low over an extended range of NW resistance values R , from ~ 1 to 100 M Ω . This range covers the transition from the linear to the sub-threshold regime. The lowest value of $2 - 3 \cdot 10^{-5}$ V/ $\sqrt{\text{Hz}}$ corresponds to a detection limit of 0.5 ‰ of a typical Nernstian pH shift in one Hz bandwidth (right axis) throughout the full resistance range (\bullet).

The data set obtained at a fixed V_{bg} and varying V_{ref} (\blacktriangle) demonstrate the cross-over between the two different regimes. In this case a very pronounced transition from a regime with low sensitivity (low R) to a regime with high sensitivity (larger R) is apparent. For this case, it has recently been pointed out⁵¹ that the signal-to-noise ratio (SNR) increases with resistance R and

is the highest in the subthreshold regime. We confirm this as well but we emphasize that the dual-gate approach used here provides a more general and detailed insight. For $V_{\text{ref}} = -0.3$ V, the contact leads also contribute to the total noise and strongly increase δV_{th} . In contrast, for $V_{\text{ref}} = +0.5$ V, the resistance of the NW-FET is not contact-dominated. In that case the noise is constantly low over the whole resistance range.

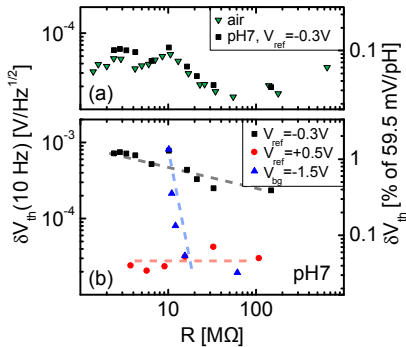


Figure 3.4: Threshold voltage fluctuations $\delta V_{\text{th}} = S_V / (\ln G(V_{\text{bg}}))'$ (a) and $S_V / (\ln G(V_{\text{ref}}))'$ (b), calculated from the data in Figure 3.3 as a function of R . Dashed lines are guides to the eye. The right axis shows δV_{th} relative to the Nernst limit of the pH sensitivity (59.5 mV/pH at 300 K).

Now, we estimate the charge noise of the NW, which corresponds to the minimum detectable number of charge carriers on the gate. To do so, we first define the gate-referred power spectrum voltage noise $S_{\text{VG}} = \delta V_{\text{th}}^2 = S_I / g_m^2$. Here, $S_I = S_V / R^2$ is the current noise that can be easily determined from Figure 3.3, and $g_m = \partial I / \partial V_g$ denotes the transconductance with respect to the controlling gate. For the measurement versus the liquid gate ($V_{\text{bg}} = -1.5$ V), we obtain a charge noise at 10 Hz of $\sqrt{S_q} = C_{\text{lg}} \cdot \sqrt{S_{\text{Vg}}} / e \approx 5.8 e / \sqrt{\text{Hz}}$, where $C_{\text{lg}} \approx 26$ fF is the estimated liquid gate capacitance in our system and e is the elementary charge.

Recently, we have extended the noise measurements to samples with implanted contacts, fabricated according to Protocol 2 (see Appendix B). They have the advantage that the contact dominated regime is suppressed. Using such samples, we systematically study the influence of the nanowire width on the noise properties and compare different gate dielectrics, Al_2O_3 and HfO_2 . We find that the channel noise scales with the effective nanowire width as expected. When referring to the gate, the scaled voltage noise δV_{th} is independent of the nanowire width or the gate oxide type. We also find

that the gate dielectric is the dominant noise source. Our voltage noise value $\delta V_{\text{th}} \approx 10^{-5} \text{ V}/\sqrt{\text{Hz}}$, evaluated at 10 Hz in 1 Hz bandwidth for a $1 \mu\text{m}$ wide NW, is the lowest reported and at least 3 – 10 times lower than in previous studies.^{52, 54, 57} A detailed discussion of the width and oxide dependence of the noise will follow in the PhD thesis by Kristine Bedner.

3.4 Conclusions

In conclusion, we have studied the low-frequency $1/f$ noise in dual-gated Si nanowire FET sensors and determined the detection limit over a large resistance range. The deduced gate-referred threshold voltage noise δV_{th} is the true figure of merit in such sensors. We demonstrate that δV_{th} is constant over the full operation range of the transistor, as long as the intrinsic nanowire resistance dominates and the contact resistance can be neglected. Both linear and subthreshold regime can be used for equally sensitive pH measurements with a detection limit of ~ 200 ppm of a full Nernstian pH shift (1 Hz bandwidth at 10 Hz, $1 \mu\text{m}$ wide NW).

4

Surface passivation and reference electrode

So far, we have focused on the pH sensing properties of a bare oxide surface. In this chapter, we will expand our investigations to a chemically modified surface. We will cover the Al_2O_3 surface of Si NW FETs with a long alkyl chain (C 18) silane and investigate its pH sensing properties both experimentally and theoretically. These results have been published elsewhere.⁴²

4.1 Introduction

The most widely used method for chemical surface modification is the self-assembly of silane monolayers on activated (hydroxylated) oxide surfaces.⁵⁸ Surface chemistry has not only been applied to functionalize the sensor, but also to tackle another major challenge in this field – the on-chip integration of a reference electrode that only reacts to the changes of the electrostatic potential but not to the chemical one. Ideally, the reference electrode should be a transistor with very similar electrical properties as compared to the sensing device but with a passivated surface, the so called reference FET (RFET). A differential ISFET/RFET setup can then be implemented. The first RFET was a parylene-coated Si_3N_4 ISFET, introduced by Nakajima et al.,⁵⁹ but it failed to completely suppress the pH sensitivity. According to the site-binding model, the pH response is determined by the number of active surface groups N_s .³⁷ A practical upper limit for a bare oxide surface is $N_s = 10^{15} \text{ cm}^{-2}$, due to bonding distances in oxides.³⁸ One can

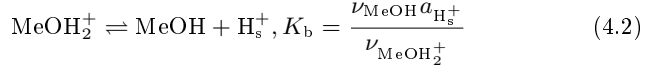
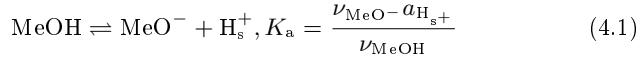
estimate that a reduction of N_s by at least three orders of magnitude is needed to eliminate the pH response.⁶⁰ It was shown that such a drastic decrease cannot be reached by chemical modification of SiO_2 and Ta_2O_5 surfaces with various short-chained silanes.³⁸ A residual pH response of the modified device was still observed ($> 10 \text{ mV/pH}$,³⁸ $> 20 \text{ mV/pH}$,¹⁴). In a work by Perrot et al.,⁶¹ two conventional FETs were used for the specific detection of Ag^+ ions in a differential mode, i.e. the sensing FET was coated with Ag-selective cyano-terminated silane, and a reference FET with an unreactive isopropyl silane. Unfortunately, both FETs were still strongly pH sensitive ($\sim 16 \text{ mV/pH}$), compared to 35 mV/pH of the bare SiO_2 . Again, only molecules with a relatively short chain length were used, but the authors were aware of a possible influence of the chain length on the pH response. Bataillard et al.⁶² applied capacitance spectroscopy to measure the pH response of a $\text{Si/SiO}_2/\text{electrolyte}$ structure, coated with silanes bearing a long, hydrophobic docosyl chain (C 22 alkyl segment). Strongly reduced pH sensitivity was reported (8 mV/pH) but the explanation was based on hydrophobicity rather than on the site-binding model.

Here, we choose octadecyldimethylmethoxysilane (ODMS) for the following reasons. First, it does not build multilayers. Since it has only one leaving group, either a dimer is formed which will not stay at the surface at all, or the silane will bind to the surface with the only available methoxy leaving group. It has been shown that a real monolayer is formed only if monoalkoxysilanes are used.⁶³ Second, we expect the long chain silanes to organize better on the surface and to be more proton-tight than the layer formed from short chain silanes.^{61,62} Third, this silane is inert once immobilized on the surface, since no reactive groups are available. In addition, we found out during this study that varying the time of the silane vapor deposition leads to a surprisingly well-controlled change of the surface coverage and hence the pH sensitivity.

4.2 The site-binding model

In the following section, we will first present the theoretical model and then discuss some of its relevant implications. Here, we use the full site-binding model (SBM), derived for conventional ISFETs by Bousse, de Rooij and Bergveld,³⁷ which provides a functional relationship between the surface potential Ψ_0 and the pH value of the bulk solution. To derive a useful expression, one has to look at the reactions of the surface hydroxide groups with the potential determining ions in the solution. The amphoteric character of the OH surface groups of a metal (Me) oxide can be expressed by two equilibrium constants for the deprotonation (K_a) and the protonation

reaction (K_b):



with ν being the number of sites of one particular species, $a_{\text{H}_s^+}$ the activity of the surface protons. The active surface sites are either neutral (MeOH), positively (protonated, MeOH_2^+) or negatively charged (deprotonated, MeO^-). The total number of these sites is

$$N_s = \nu_{\text{MeOH}} + \nu_{\text{MeO}^-} + \nu_{\text{MeOH}_2^+} \quad (4.3)$$

The protonated and deprotonated groups generate the total surface charge

$$\sigma_0 = \left(\nu_{\text{MeOH}_2^+} - \nu_{\text{MeO}^-} \right) e \quad (4.4)$$

Equation 4.4 can be rewritten using Equations 5.1 - 4.3:

$$\sigma_0 = eN_s \left(\frac{a_{\text{H}_s^+}^2 - K_a K_b}{a_{\text{H}_s^+}^2 + a_{\text{H}_s^+} K_b + K_a K_b} \right) \quad (4.5)$$

The surface charge σ_0 is screened by the ions of the double layer, leading to a surface potential drop Ψ_0 over the double-layer capacitance C_{dl}

$$\sigma_0 = C_{\text{dl}} \Psi_0 \quad (4.6)$$

In order to get a convenient expression, the (unknown) activity of the surface protons in Equation 4.5 has to be replaced by the (known) activity of the bulk solution protons $a_{\text{H}_b^+}$ via the Boltzmann equation

$$a_{\text{H}_s^+} = a_{\text{H}_b^+} \exp\left(-\frac{e\Psi_0}{kT}\right) \quad (4.7)$$

Combining Equations 5.1 - 4.7, an explicit relationship between the bulk proton activity $a_{\text{H}_b^+}$ and the surface potential Ψ_0 can be derived

$$a_{\text{H}^+} = \sqrt{K_a K_b} \exp\left(\frac{e\Psi_0}{kT}\right) \times \quad (4.8)$$

$$\frac{\frac{e\Psi_0}{kT} \frac{C_{\text{dl}}}{C_s} \frac{1}{2} \sqrt{\frac{K_b}{K_a}} + \sqrt{1 + \left(\frac{e\Psi_0}{kT} \frac{C_{\text{dl}}}{C_s} \frac{1}{2} \sqrt{\frac{K_b}{K_a}}\right)^2} \left(1 - \left(2\sqrt{\frac{K_a}{K_b}}\right)^2\right)}{1 - \frac{e\Psi_0}{kT} \frac{C_{\text{dl}}}{C_s}}$$

in which the surface buffer capacitance C_s is related to the number of sites N_s via

$$C_s = \frac{e^2 N_s}{2.3kT} \quad (4.9)$$

In contrast to Bousse et al.,³⁷ Equation 4.9 is not further simplified. First, the theoretical predictions of Equation 4.9 are discussed. In Figure 5.1, we plot the surface potential Ψ_0 vs. the pH of the bulk solution, according to Equation 4.9. The point of zero charge PZC = $(\text{p}K_a + \text{p}K_b)/2$ is set to $\text{pH} = 7$. The double layer capacitance C_{dl} at a constant ionic strength of 100 mM is estimated as a series connection of the Stern layer C_{st} and the diffusive layer capacitance C_{dif} to $C_{\text{dl}} = C_{\text{dif}} C_{\text{st}} / (C_{\text{dif}} + C_{\text{st}}) \approx 0.16 \text{ F/m}^{-2}$, including the widely accepted constant $C_{\text{st}} = 0.2 \text{ F/m}^{-2}$.^{14,37,64} The capacitance of the diffusive layer $C_{\text{dif}} = 0.7 \text{ F/m}^{-2}$ is estimated assuming a simple parallel plate capacitor. The pH dependence of C_{dl} , estimated by Chen et al.,¹⁴ is only a small effect and is neglected in the following. As illustrated in Figure 5.1a, for a large number of surface sites ($N_s > 10^{14} \text{ cm}^{-2}$) and a small separation between the reaction constants $\Delta\text{p}K = \text{p}K_a - \text{p}K_b$, the surface potential decreases linearly with increasing bulk pH. Here, the smallest possible $\Delta\text{p}K = 0$ was chosen, which gives the steepest slopes of the straight lines (58.8 mV/pH for 10^{15} cm^{-2} and 56.9 mV/pH for 10^{14} cm^{-2}). These slopes or pH sensitivities are very close to the Nernst limit. It was already pointed out by Fung et al. that the highest pH sensitivity of an ISFET is expected for a combination of large N_s and small $\Delta\text{p}K$ values.⁶⁴ Further reducing N_s yields a sigmoid (or S-shaped) curve (10^{13} cm^{-2}) with its steepest slope around the PZC, which becomes almost flat for 10^{12} cm^{-2} . Hence, a reduction of N_s by at least three orders of magnitude is needed to get a pH insensitive surface. To see the relationship between Ψ_0 and N_s more clearly, we have made several cuts along the lines of constant pH, for example along the vertical dashed line at $\text{pH} = 5$. The inset shows such cuts, Ψ_0 as a function of N_s , for five different pH values between 3 and 7 (\leq PZC). Again, no potential shift due to pH change is observed below $N_s = 10^{12} \text{ cm}^{-2}$, while at $N_s > 10^{14} \text{ cm}^{-2}$ a nearly Nernstian response is visible. Note that Ψ_0

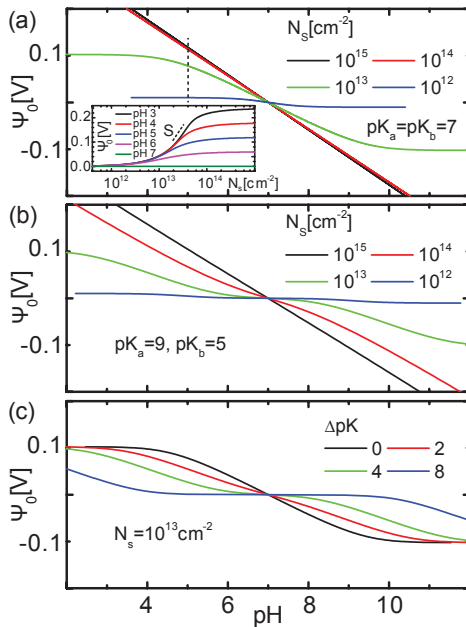


Figure 4.1: Theoretical curves of the surface potential Ψ_0 vs. the pH of the bulk solution (~ 100 mM ionic strength), as predicted by the full site-binding model for a surface with PZC = 7, see 4.9. In (a), the deprotonation and protonation constants pK_a and pK_b are both set to 7 ($\Delta pK = 0$). The total number of surface sites N_s is varied. Inset: Ψ_0 vs. N_s at different pH values. Each curve is a cut along the line of a constant pH in the main figure, for example at $\text{pH} = 5$ (shown by the vertical dashed line). The steepest slope $S = \delta\Psi_0/\delta N_s$ is taken to estimate the minimum detectable change δN_s due to the adsorption of target molecules on the sensor surface. In (b), a $\Delta pK = 4$ is assumed, for otherwise the same parameters as in (a). (c) Influence of $\Delta pK = pK_a - pK_b$ on the curve shape at a constant and low N_s (partially passivated surface).

vs. N_s curves are also S-shaped with the largest variation in the range of $10^{13} - 10^{14} \text{ cm}^{-2}$. The steepest slope $S = \delta\Psi_0/\delta N_s$ is strongly pH dependent, it is zero at the PZC and increases when moving away from $\text{pH} = 7$. The quantity S will be used later to estimate the minimum detectable change δN_s due to the adsorption of target molecules on the sensor surface.

The above definition of the pH sensitivity, i.e. the slope of a straight line, only makes sense in the linear response range, which can be quite narrow depending on the parameters. To make the comparison between the different curves easier, we introduce here an average pH sensitivity s_{pH} .

All the SBM curves are nearly saturated below a certain $\text{pH}_{\text{sat}1}$ and above $\text{pH}_{\text{sat}2}$. Reading out the difference Ψ_0 between the asymptotes at these saturation values gives the maximum potential shift $\Delta\Psi_{0,\text{max}}$. If we divide $\Delta\Psi_{0,\text{max}}$ by the separation of the saturation values, we get an average pH sensitivity

$$s_{\text{pH}} = \Delta\Psi_{0,\text{max}}/(\text{pH}_{\text{sat}2} - \text{pH}_{\text{sat}1}). \quad (4.10)$$

We will use s_{pH} as a measure for the pH sensitivity in the following. For a larger $\Delta\text{p}K = 4$, assuming that the protonation is more likely to happen than the deprotonation (i.e. $K_{\text{a}} < K_{\text{b}}$ or $\text{p}K_{\text{a}} > \text{p}K_{\text{b}}$), the full Nernstian slope cannot be reached any more (Figure 5.1b). For $N_{\text{s}} = 10^{15} \text{ cm}^{-2}$, the pH sensitivity is reduced to 53.2 mV/pH and is non-linear already for 10^{14} cm^{-2} and below. Note that the shape of the curve has changed as well. It is relatively flat around the PZC and has the steepest slopes at the pK values (double-sigmoid shape). The transition from the sigmoid to the double-sigmoid shape is best seen in Figure 5.1c. In this plot, N_{s} is kept constant and low at 10^{13} cm^{-2} to ensure a clearly non-linear behavior. With increasing separation $\Delta\text{p}K$, the flat region around the PZC gets broader and the curve shape changes from sigmoid to double-sigmoid, saturating at more extreme pH values.

The transition from the linear pH response to the sigmoid shape is determined by the ratio $C_{\text{dl}}/C_{\text{s}}$ (cf. Equation 4.9), where C_{s} is the buffer capacitance of the surface and is proportional to the number of sites N_{s} , see 4.9. In principle, variations of either C_{dl} or N_{s} could cause this transition, by changing the capacitance ratio in Equation 4.9. However, for sufficiently strong electrolytes used here ($>100 \text{ mM}$), the double layer capacitance is nearly independent on the ionic strength, as the Stern layer capacitance C_{st} dominates. As stated above, we assume a constant $C_{\text{st}} = 0.2 \text{ F/m}^{-2}$, in agreement with previous studies. For a bare oxide surface with a large buffer capacitance, like Al_2O_3 used here, $C_{\text{s}} \gg C_{\text{dl}}$. The oxide surface has a sufficient number of OH groups that buffer the change in the bulk pH by taking up or giving away protons. If the buffer capacitance is dramatically reduced, e.g. by a chemical surface passivation, then $C_{\text{dl}} \sim C_{\text{s}}$. Changing the bulk pH uses up the available OH groups, a potential shift is still observed around each pK value, until all groups are occupied and no potential shift is visible any more. The Ψ_0 vs. pH curves saturate, resulting in an overall sigmoid shape if pK values are close to each other or in a double-sigmoid shape if they are further apart.

4.3 Experimental results and comparison with model

Now, we go on by presenting our experimental results and the fits to the data obtained using the model discussed above. The NW samples (Structure B, see Chapter 1) were fabricated according to Protocol 1 or 2 (Appendix A or B), and silanized as described in the following. A sketch of the reaction can be found in Figure 4.2 a. Prior to the silanization, the samples were cleaned with ethanol and the surface was activated by a UV/ozone treatment (20 min). The sample surface was then modified by the deposition of octadecyldimethylmethoxysilane (ABCR, AB111258) vapor at 80 °C and ca. 0.05 mbar. The reaction time varied between 6 hours and 7 days. After the reaction, the samples were cured at 80 °C for two hours. Control samples (i.e. roughly 1 cm² large Si wafer pieces) were silanized in parallel and used immediately after curing to measure the contact angle.

All samples were characterized before functionalization in ambient and in liquid showing good transistor behavior and nearly Nernstian pH response. An example of a measured transfer curve of a fully passivated NW (after 7 days of reaction) is depicted in Figure 4.2 b on a semi-log plot. The electrical properties of the transistor, especially the hysteresis and the subthreshold swing, are not significantly altered by the surface chemistry. The sensor responds to pH change by a shift of its threshold voltage V_{th} . We define this quantity as the V_{ref} value at a constant NW conductance G in the subthreshold regime, e.g. 10 nS (horizontal line in Figure 4.2 b). The mean V_{th} value from the up and down gate sweep is taken.

To get some information about the reaction progress, contact angle measurements were performed on silicon test wafer pieces (≈ 1 cm² in size) that were processed together with the NWs. In Figure 5.2a, the contact angle (CA) data from the test samples are plotted against the passivation time. Both silica (standard thermal growth; squares) and alumina surfaces (grown by atomic layer deposition, ALD; circles) were used. The latter was produced the same way as the active gate dielectric of the NW. The solid lines are guides to the eye. A rapid increase of the CA from zero (freshly activated surface) to 70° – 80° is observed within the first hours. After several days, CA saturates at around 102° – 105°, conclusively showing a hydrophobic surface nature. This value corresponds to a nearly full surface coverage for this type of silane and is in agreement with previously published results obtained with comparable systems.^{65,66} Note that the hydrophobicity is an important requirement for a proton-tight surface. The advantage of such a slow (several days) reaction is that the number of active surface sites can be controlled very well by varying the reaction time.

Several samples (with 48 nanowires each) were used for the experiment, all showing consistent results. No significant influence of the NW width (100–

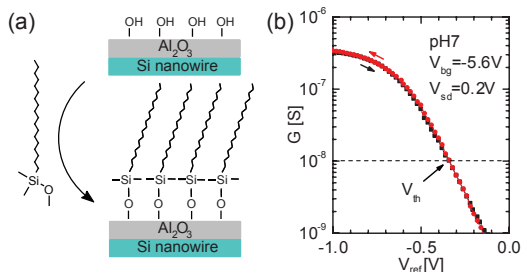


Figure 4.2: (a) The chemical modification of an activated Al_2O_3 surface (20 min UV/ozone) was performed by vapor deposition of octadecyldimethylmethoxysilane (at 80°C , ~ 0.05 mbar). The reaction time was varied from six hours to seven days. (b) Conductance G vs. V_{ref} of a fully passivated NW (transfer curve). There is no significant change of the subthreshold swing upon passivation. Short arrows indicate the gate sweep direction. Almost no hysteresis is observed. Threshold voltage V_{th} (indicated by long arrow) is defined in the subthreshold regime at a constant G value (dashed line). Average value from both gate sweeps is taken to compute V_{th} .

1000 nm) on the pH sensitivity is observed. All the samples were silanized more than once to try different passivation times. The surface can be regenerated either by a UV/ozone cleaning (>20 min) or by a gentle oxygen plasma treatment without damaging the NWs.⁶⁷ In Figure 5.2b, the measured threshold voltage difference $\Delta V_{\text{th}} = V_{\text{th}}(\text{PZC}) - V_{\text{th}}$ is depicted as a function of pH for different passivation times (solid squares).⁶⁸ Without the silane (0 d), a linear dependence can be observed, with a nearly Nernstian slope of 60 mV/pH (solid line). After one day of silanization (1 d), the pH response is clearly weaker and non-linear, saturating below $\text{pH}_{\text{sat}2} = 3$ and above $\text{pH}_{\text{sat}1} = 11$. The same sample was cleaned and silanized for 3 d, showing strongly suppressed pH sensitivity while keeping the non-linear shape. Even more striking is the result of a second sample, passivated for 7 days. The pH response is rather flat with some scattering ($-3 \pm 4 \text{ mV/pH}$), but can be almost fully restored after an oxygen plasma treatment⁶⁷ (55 mV/pH , empty squares). To our knowledge, this is the first time that a pH sensitivity reduction of an ISFET-type device clearly below 10 mV/pH is demonstrated by silanization. We stress that the usually highly pH-sensitive Al_2O_3 surface is only covered by a single monolayer of silanes. The non-linear curves were fitted using Equation 4.9. The point of zero charge is assumed to be at $\text{pH} = 7$, since the measured curves are quite symmetric around this value. The reported PZC values of Al_2O_3 -ISFET range between $\text{pH} 4.2$ and 9 .⁶⁹ Since a single sigmoid shape is observed in the experiment and the pH sensitivity of the bare alumina surface is close to the Nernst limit, a small separation of

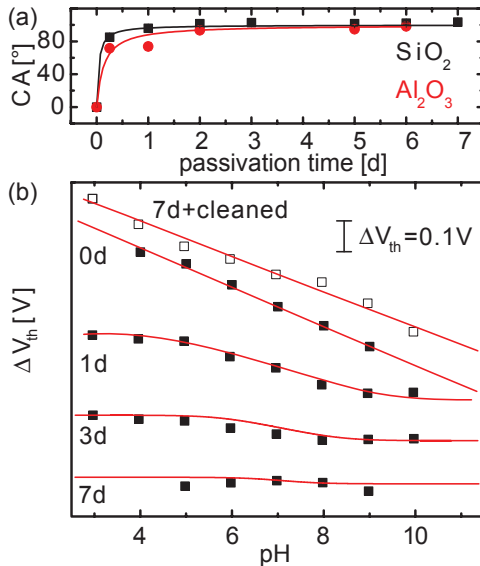


Figure 4.3: (a) Contact angle (CA) of a water droplet on a test wafer surface (SiO_2 , squares; Al_2O_3 , circles) as a function of the passivation time in days. Solid lines are guides to the eye. (b) Threshold voltage difference ΔV_{th} of Al_2O_3 -coated Si NWs vs. pH of the buffer solution for several reaction times (from top to bottom: 0 to 7 days, solid squares). Empty squares show the data for a fully passivated sample after plasma cleaning. Straight lines are linear fits (60 mV/pH for 0d, 55 mV/pH for 7 days then cleaned); non-linear curves are fits of the site-binding model with following parameters: $\Delta pK \approx 0.4$, $C_{dl} = 0.16 \text{ F/m}^{-2}$) and varying N_s . Curves are shifted for clarity.

the ionization constants ΔpK is needed to optimize the fits. We have found that $\Delta pK \approx 0.4$ gives a very good fit for all curves. This separation is closer to the ideal value of zero than the recently reported $\Delta pK \approx 1.5$.¹⁴ The double-layer capacitance is set to $C_{dl} = 0.16 \text{ F/m}^{-2}$, based on the literature values.⁷⁰ Keeping these numbers constant, the only remaining free fitting parameter is the number of sites N_s , which will tell us how many groups are actually passivated.

Derived from the fits, the average pH sensitivity s_{pH} , see Equation 4.10, is plotted in Figure 4.4a (left vertical axis and squares), together with N_s (right vertical axis and circles). Note that the same $\text{pH}_{sat1} = 3$ and $\text{pH}_{sat2} = 11$ were taken for all SBM curves to compute s_{pH} according to Equation 4.10. Both s_{pH} and N_s monotonically decrease with the passivation time, proving that our surface modification method provides reliable results and is well-

controlled. The data after 7 d were fitted using $N_s = 10^{12} \text{ cm}^{-2}$,⁷¹ which corresponds to a decrease of the active groups by 800 times as compared to the literature value for the bare alumina surface ($N_0 = 8 \times 10^{14} \text{ cm}^{-2}$, see e.g.¹⁴).

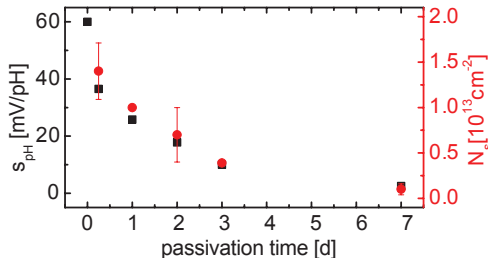


Figure 4.4: Average pH sensitivity s_{pH} (left axis and squares; defined in the text) and number of active surface sites N_s (right axis and circles) vs. the passivation time. N_s is obtained from the fits of the site-binding model, as shown in 5.2.

Finally, we estimate a detection limit of our sensing platform, since we would like to know how many molecules of an analyte are required to give the smallest measurable signal difference. Usually, the application of an ISFET is limited to sensing of charged analytes. A different approach is needed to detect neutral species. If such uncharged species, like the silane used here, adsorb on the sensing surface, they will cause a change of the number of active sites δN_s . This will also result in a surface potential shift $\delta\Psi_0$, see Figure 5.1a. A sensitivity to the change in the number of groups can be defined as $S := \delta\Psi_0/\delta N_s$. This number corresponds to the slope of the curves shown in Figure 5.1a (inset). Note that the strongest response occurs in the range of $N_s = 10^{13} - 10^{14} \text{ cm}^{-2}$, where the surface is partially passivated. In a real setup, the threshold voltage shift δV_{th} is measured rather than $\delta\Psi_0$. The minimum detectable δV_{th} is limited by the low frequency $1/f$ noise below $f = 1 \text{ kHz}$.⁴⁵ The change in N_s must therefore lead to a potential shift larger than the noise limit in order to be detected by the sensor. If taken at pH = 6, the steepest slope is $S \approx 10^{-19} \text{ Vm}^2$, see Figure 5.1a (inset), and we estimate a detection limit of $\delta N_s = \delta V_{\text{th}}/S \approx 10^{-4} \text{ VHz}^{-1/2}/10^{-19} \text{ Vm}^2 \approx 1000 \mu\text{m}^{-2}\text{Hz}^{-1/2}$ for a typical sensor surface of $\sim 1 \mu\text{m}^2$. The value for the threshold voltage noise δV_{th} was taken from our previous work⁴⁵ and assumes a time scale of 10 Hz for the surface interactions. For a ten times slower process (1 Hz), δN_s rises due to a larger $1/f$ noise by a factor of $\sqrt{10} \approx 3.2$. If we go further away from the PZC, e.g. to pH = 3, then S increases to $\sim 6 \times 10^{-19} \text{ Vm}^2$ which gives even a smaller value of $\delta N_s \approx 170 \mu\text{m}^{-2}\text{Hz}^{-1/2}$

at 10 Hz.

4.4 Conclusions

To conclude, the highly pH sensitive alumina surface of silicon nanowire field-effect transistors has been modified by vapor deposition of a silane with a long alkyl chain (C 18). A gradual decrease of the pH response was observed with increasing surface coverage, which was modified in a controlled way by changing the deposition time. The full site-binding model was used to describe the results quantitatively. The number of active surface sites was derived from the fits of the model to the experimental data. As the number of active sites goes down, the shape of the sensor response to pH changes from linear to sigmoid to flat, because the surface loses its buffering capacitance. A reduction of active surface groups N_s by three orders of magnitude was achieved after seven days of silanization, resulting in a practically pH insensitive surface. Since the electrical properties of the fully passivated nanowires are barely changed by the molecular monolayer, such nanowires could be used as pH reference electrodes in a differential measurement setup. Finally, we have also shown that a partially passivated surface can be sensitive to changes in N_s caused by the adsorption of uncharged species. This sensitivity $S = \delta\Psi_0/\delta N_s$ is optimized if the measurement is performed at a pH value far away from the point of zero charge of the surface. A detection limit for this type of application was estimated.

5

Understanding the electrolyte background for biochemical sensing

Previous chapters dealt with various aspects of pH sensing. Here, we will vary the ionic strength of the electrolyte background at different constant pH values and see how this influences the sensor response. The experimental data will be compared with theoretical models. These results have been submitted for publication.⁷²

5.1 Introduction

Over the past decades, interfaces between oxides and electrolytes have received considerable attention in different scientific communities. In particular, the adsorption of inorganic salt ions on colloidal oxide surfaces has been extensively studied^{73–78} and reviewed.^{79,80} The adsorption mechanism was explained within the site-binding model (SBM)^{35,36,81} by the surface complexation of ions with oppositely charged oxide sites. Apart from colloid science, a description of the oxide/electrolyte interface has been essential for the development of glass electrodes (GE). Recently, researchers celebrated the centenary of GEs and the related Nikolsky's ion exchange theory, which is widely used to describe not only GEs but also other ion-sensitive electrodes.^{82–84} In the 1970s, the ion-sensitive field-effect transistors (ISFETs) emerged, combining the properties of a transistor with a GE-like interface.³⁴

Nikolsky's theory was quite naturally used to explain the experimental results obtained with ISFETs.^{85,86} However, the Nikolsky-Eisenman equation is semi-empirical and its use is limited to estimating the selectivity of a sensor against interfering ions. To give a more detailed theoretical explanation, the successful SBM was later adapted to ISFETs^{37,64} and simplified in the following years by P. Bergveld and co-workers.^{1,39,87} With the rise of nano-scaled ISFETs,⁸⁸⁻⁹⁰ the attention has again been drawn to the interactions between the active oxide surface and the ions in the electrolyte. Even though many pH measurements with nanowire-based ISFETs have been reported, for example,^{11,13,14} surprisingly few attempts to measure changes in electrolyte concentration with miniaturized ISFETs have been published so far, with inconsistent results.^{29,47,52,91,92} More specifically, Nikolaides et al.⁹¹ and Park et al.²⁹ reported a weak non-linear response of a SiO₂-coated FET to KCl or NaCl. In contrast, Clément et al. claimed a full linear Nernstian response of around 60 mV/dec to NaCl, using SiO₂-coated nanowire ISFETs. Unfortunately, none of these studies has performed a quantitative assessment of the data using a theoretical model. Recently, Zafar and co-workers⁴⁷ measured HfO₂-covered Si nanowires and did not observe any appreciable response up to 1 M NaCl. In our previous paper,⁴¹ we showed that a miniaturized ISFET with an Al₂O₃ interface only weakly responds to various types of ions up to a moderate concentration of 10 mM, at a constant pH \approx 6. The results of both studies^{41,47} were qualitatively described by the Bergveld model.¹ In the following, we significantly expand our recent study by using silicon nanowires coated with high-k HfO₂ and Al₂O₃ to systematically measure their response to changes in KCl concentration up to 1 M, at several constant pH values.

5.2 Results and discussion

All samples were first characterized as pH sensors. In Figure 5.1 a, conductance G vs. V_{ref} of an Al₂O₃-coated sample is shown on a semi-log plot. The subthreshold swing SS is around 100 mV/dec (dashed line). To quantify the shifts of the transfer curve, we read out the threshold voltage V_{th} as the value of V_{ref} at a constant conductance $G = 20$ nS (along the arrow). In addition to the results presented in Chapter 2, we plot V_{th} as a function of pH for 3 different total ionic strengths of the electrolyte (Figure 5.1 b, Al₂O₃). All three datasets show a similar behavior. The threshold voltage shifts linearly with pH, exhibiting a nearly Nernstian response of ~ 56 mV/pH (dashed lines). It is important to realize that the relative shifts ΔV_{th} are independent of the ionic strength. We will come back to this point later. Similar results were obtained with a HfO₂-coated sample.

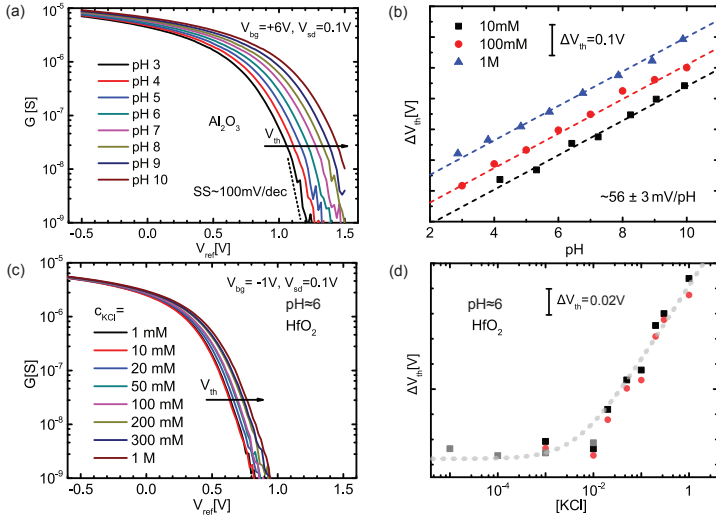
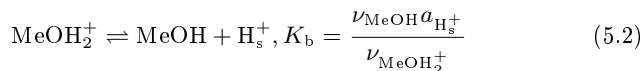
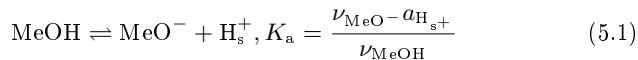


Figure 5.1: (a) Conductance G vs. V_{ref} for an Al_2O_3 -coated nanowire on a semi-log plot (same data as in Figure 4.2 e). The subthreshold swing SS is around 100 mV/dec . The pH response is quantified by the shift of the threshold voltage V_{th} upon a change in pH. We read out the threshold voltage V_{th} as a value of V_{ref} at a constant $G = 20 \text{ nS}$ (along the arrow). The threshold voltage shift ΔV_{th} as a function of pH is shown in (b) for three different ionic strengths of the electrolyte. ΔV_{th} is a linear function of pH with the slope of $\sim 56 \text{ mV/pH}$ (indicated by dashed lines). No significant dependence of the slope on the ionic strength is found. (c) Transfer curve of a HfO_2 -coated nanowire for different concentrations of the electrolyte $\geq 1 \text{ mM}$ but at a constant $pH \approx 6$. V_{th} shifts to more positive values with increasing ionic strength. This indicates the adsorption of negatively charged ions (chloride). (d) Threshold shift ΔV_{th} vs. KCl concentration read out from the measurement shown in c (dark squares), from a different measurement with the same wire (light squares), and from a different nanowire with nominally the same dimensions (circles). A non-linear behavior is observed. The dashed line is a guide to the eye.

In the next paragraphs, we will be dealing with a different type of experiment, namely varying the KCl concentration in deionized water. In Figure 5.1 c, the results of a HfO_2 sample are plotted. The pH value of all solutions was ≈ 6 . The curves shift to more positive gate values with increasing ionic strength. In contrast to the pH measurement, the V_{th} shift to salt is non-linear (see Figure 5.1 d). Up to 10 mM, almost no shift occurs, as we have already reported (Chapter 2 and Ref.⁴¹). Above this value, the nanowire starts responding strongly to the changes in ionic strength (up to full Nernstian response). Because V_{th} shifts towards more positive values, we conclude that the effect must be due to the adsorption of negative ions, that is chloride Cl^- . Moreover, this effect does not show any significant pH dependence, and is very similar for both HfO_2 and Al_2O_3 interface, as we will see in the following.

In Figure 5.2 a-c, the experimental results for a HfO_2 -coated sample (solid symbols) are compared with three existing models (lines). Note that on the horizontal axis, the KCl concentration c_{KCl} was replaced by the activity a_{Cl^-} , which was estimated using the specific ion interaction theory (SIT), see for example.⁹³ This correction is needed because the approximation $c_{\text{KCl}} \approx a_{\text{Cl}^-}$ is no longer valid at high ionic strength due to interaction between the electrolyte ions. On the vertical axis, the measured threshold voltages V_{th} were converted to surface potential via $\psi_0 = V_{\text{th}}(\text{PZC}) - V_{\text{th}}$, where $V_{\text{th}}(\text{PZC})$ is the threshold voltage at the assumed point of zero charge (PZC). Based on previously published studies, we have chosen $\text{PZC} = 7$ for HfO_2 (a-d)⁹⁴ and $\text{PZC} = 8$ for Al_2O_3 (e).^{14,80} The resulting ψ_0 is zero at $\text{pH} = \text{PZC}$, positive at $\text{pH} < \text{PZC}$ and negative at $\text{pH} > \text{PZC}$. We observe that the measured data points move to more negative ψ_0 with increasing KCl concentration, irrespective of the pH value. As mentioned before, this indicates the adsorption of negatively charged species.

The most obvious model to start the comparison with is the site-binding model, which was derived in the previous chapter. In Figure 5.2 a, fits of a simple SBM with are shown, in which the surface potential is determined by protonation or deprotonation of the amphoteric surface groups:



where Me denotes a metal, H_s^+ a surface proton, ν the number of particular sites, $a_{\text{H}_s^+}$ the activity of surface protons, K_a and K_b the dissociation and association constant, respectively. Based on these equations, the response to

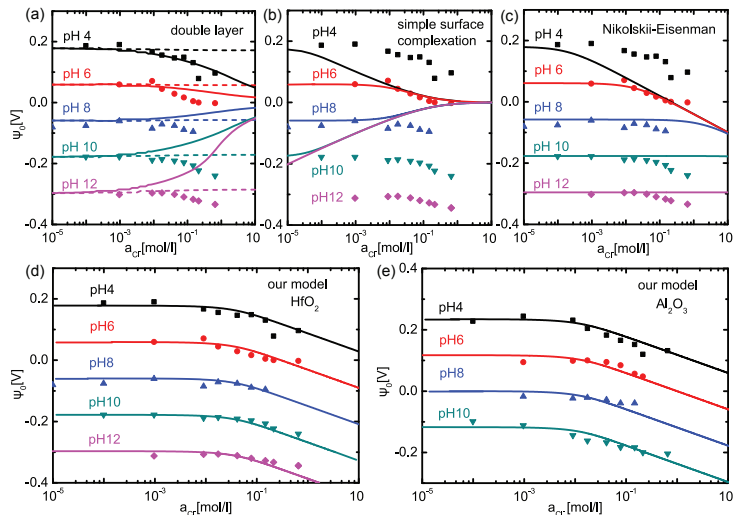
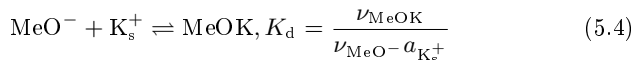
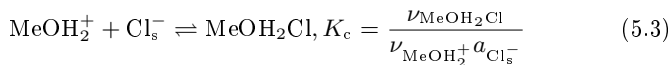


Figure 5.2: Plots of the surface potential ψ_0 versus the activity of the chloride ions in the bulk solution a_{Cl^-} . Solid symbols represent experimental data points for a HfO_2 -coated (a–d) and an Al_2O_3 -coated sample (e), whereas lines are theoretical fits based on different models. The measured threshold voltages V_{th} were converted to surface potential via $\psi_0 = V_{\text{th}}(\text{PZC}) - V_{\text{th}}$. The point of zero charge is set to $\text{PZC} = 7$ for HfO_2 (a–d) and $\text{PZC} = 8$ for Al_2O_3 (e). We observe that the measured data points move to more negative ψ_0 with increasing a_{Cl^-} , irrespective of the pH value. This implies the adsorption of negatively charged species on the surface. (a) Fits of the double-layer capacitance model with parameters from literature (dashed lines) and the best fitting parameters (solid lines). In this model, the ionic strength changes the surface potential via the double-layer capacitance. In (b), the electrolyte ions contribute to ψ_0 by a complexation reaction with the oppositely charged surface groups. (c) Fits of the well-known Nikolskii-Eisenman equation. The only changing parameter from curve to curve is the proton activity. All other parameters are fixed, unlike previous works. (d) In contrast to the fits shown in (a–c), our model describes the complete data set for all pH values. (e) Similarly good agreement between experiment and model was achieved for a Al_2O_3 -coated sample.

pH can be described by an analytical expression $a_{\text{H}^+}(\psi_0)$ with two key parameters: the surface buffer capacitance C_s and the double-layer capacitance C_{dl} (see Chapter 4). We remind that the buffer capacitance is the ability of the surface to give away or take up protons which is determined by the density of active surface sites (OH groups). The higher the C_s , the more linear and closer to the Nernstian value is the pH response. In this approach, the electrolyte ions can influence the potential via the Debye screening length, which enters the double-layer capacitance $C_{\text{dl}} = C_{\text{dif}}C_{\text{st}}/(C_{\text{dif}} + C_{\text{st}})$, where C_{st} is the constant Stern layer capacitance and C_{dif} is the differential capacitance, mainly determined by the ionic strength. However, the influence is very small (dashed lines) if literature values for $C_{\text{st}} = 0.2 \text{ F/m}^{-2}$ and the number of active sites $N_s = 10^{19} \text{ m}^{-2}$ are taken.^{14,37,42,64} Especially C_{st} proves to be the limiting factor, because it leads to saturation of C_{dl} at $\approx 0.16 \text{ F/m}^{-2}$. If we increase C_{st} to 20 F/m^{-2} and reduce N_s somewhat to $4 \times 10^{18} \text{ m}^{-2}$, the influence of ionic strength can become pronounced (solid lines). However, as only the data at pH = 4 can be fitted nicely, two major difficulties of this model become obvious. First, the SBM predicts a sign change of the effect, i.e. the curves bend downwards if $\text{pH} < \text{PZC}$ and upwards if $\text{pH} > \text{PZC}$. In other words, if the surface is, for instance, positively charged (pH 4 and 6), only negative ions are attracted, neutralizing the surface charge. Analogously, a negative surface (pH 8, 10, 12) attracts positively charged electrolyte ions. The latter case was not observed in the experiment, despite covering a wide pH range. The second problem of the model is that the pH response, i.e. the separation between the five solid curves, gets smaller with increasing ionic strength. A fully Nernstian behavior only occurs at low activities $a_{\text{Cl}^-} < 10^{-3} \text{ mol/l}$, whereas at 1 M, for example, the model predicts a weak and non-linear pH response of roughly 25 mV/pH. This also strongly disagrees with the experiment shown in Figure 5.1 b, in which nearly ideal pH response was observed even at 1 M background concentration.

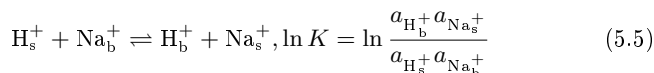
Another way of including the electrolyte ions in the SBM is by writing down two additional equations for the so-called surface complexation:



Combining the reactions Eq. 5.1 – 5.4, new analytical functions $a_{\text{Cl}^-}(\psi_0)$ and $a_{\text{K}^+}(\psi_0)$ can be derived. The best fits are shown in Figure 5.2 b using the following parameters: $K_a = K_b = 10^{-7}$, $K_c = K_d = 5 \times 10^{-4}$, number of active surface sites $N_s = 10^{19} \text{ m}^{-2}$. The double-layer capacitance was

set to a constant value $C_{dl} = 0.16 \text{ F/m}^2$, as discussed before.⁴² Like in the previous case, huge discrepancies appear between experiment and model. In fact, there is even a third difficulty: the activity at which the curves start to bend now depends on pH. This can be explained as follows: when the surface is strongly charged (far away from PZC), the equilibrium in Equations 5.3 and 5.4 is shifted to the right side. Electrolyte ions are easily attracted and cause a significant effect on the surface potential. In contrast, when only few charged sites are available close to the PZC, a much higher ionic strength is needed to shift the equilibrium towards products and to neutralize the remaining sites.

Instead of the SBM, Nikolsky's ion exchange theory is often used to describe the basic chemistry at the surface of a (glass) electrode, with the most prominent example being as follows:



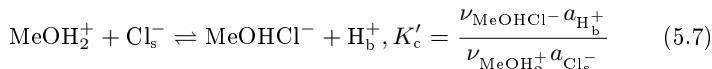
where K is the exchange constant, the subscript "b" denotes activities and ions in bulk solution, and "s" stands for surface. The semi-empirical Nikolsky-Eisenman equation can then be derived, which is often used to determine the selectivity of an ion-sensitive electrode to an interfering ion B with respect to the primary ion A:

$$V = \text{const.} + \frac{RT}{F} \ln(a_A + K a_B) \quad (5.6)$$

where V is the measured voltage, R the gas constant, T the absolute temperature, F the Faraday constant, a_A the activity of the primary ion (here: $A = \text{Cl}^-$), a_B the activity of the interfering ion ($B = \text{OH}^-$), and K is the exchange constant. The best fits can be found in Figure 5.2 c. All curves share the same set of parameters, except for the proton activity. The proton activity has a two-fold impact on the fitted curves: first, it determines the vertical position of the flat part relative to PZC; and second, it fixes the position at which the transition from the flat to the linear part takes place. Again, only the data at $\text{pH} = 6$ is described well by the model. The only way to fit the whole data set is to let the constant K act as a free fitting parameter. This would compensate the shift of the transition point caused by the proton activity, as mentioned before. This is a popular approach, the "constant" K is often called "selectivity coefficient", which depends on the pH value and is treated as a free fitting parameter (see for example,^{86,92}). The fact that K has to be adjusted with respect to pH indicates that K is ill-defined as a reaction constant. Interestingly, we found that $K/a_{\text{pH}} \approx \text{const.}$ In other words, if the proton activity is changed by a factor of ten (Δ

pH = 1), K has to be changed by ten times as well to keep the same quality of the fitting. Treating the constant K as a free fitting parameter might optimize the fits to the data and provide some numbers for the selectivity, but it is not satisfactory from the physical point of view.

Based on the above considerations, we have decided to modify the site-binding model to better fit the whole data set. We found that a slight change of the reaction equation leads to an excellent agreement between experiment and model for both HfO_2 (Figure 5.2 d) and Al_2O_3 (Figure 5.2 e). The new equation, in addition to Eq. 5.1 and 5.2, is as follows:



with K'_c being a real reaction constant (i.e. pH independent). We deduced a value of $K'_c \approx 3.3 \times 10^{-6}$ from the fits. The remaining parameters were set as follows: $K_a = K_b = 10^{-7}$, $N_s = 10^{19} \text{ m}^{-2}$, $C_{\text{dl}} = 0.16 \text{ F/m}^2$. The Equation 5.7 implies that a chloride ion from the solution forms a complex with the surface hydroxyl groups and replaces a proton at the surface, which goes to the bulk solution. This interesting insight can be further supported by recent molecular dynamics simulations of an oxide/electrolyte interface similar to ours.⁹⁵ In particular, the authors showed that the first water layers organize on the surface of oxidized aluminum via hydrogen-bonding. If NaCl solution was added to the model, the first monolayer of water was disturbed by the electrolyte. Chloride ions displaced water molecules that were originally bound to the surface. As a result, Cl^- adsorbed as inner-sphere complexes, directly interacting with the surface hydroxyl groups. The attractive interaction $(\text{O})\text{-H} \cdots \text{Cl}^-$ can reasonably be described as hydrogen bonds.⁹⁶ In contrast, the alkali ions did not displace any adsorbed surface waters and stayed at a larger distance to the surface.

5.3 Conclusions

To conclude, we have studied the response of HfO_2 and Al_2O_3 -coated silicon nanowire field-effect sensors to KCl at several pH values. A significant signal change is observed only at high ionic strengths $> 10 \text{ mM}$, with both oxides behaving very similarly. Our measurements indicate that only Cl^- ions are adsorbed on the surface, independent of the pH value. This result strongly contradicts the established site-binding model, which predicts that both types of ions can be adsorbed depending on the surface charge (or pH). Within the site-binding model, neither a double-layer effect nor a simple surface complexation can explain our observations. Moreover, the widely used Nikolsky-Eisenman equation cannot satisfactorily describe the data in

a physically meaningful way. We suggest a new model instead, which gives excellent quantitative agreement with the experimental data. According to our model, the chloride ions directly interact with the hydroxyl surface groups and replace previously adsorbed protons from the surface. Recently published molecular dynamics simulations further support our model.⁹⁵

In our opinion, these results are relevant for any type of biochemical sensing applications where the electrolyte concentration might vary, for instance, due to some biological processes. The background effects of the electrolyte ions have to be understood and clearly separated from the signals caused by the actual analyte. Even slight changes of the ionic strength in the physiological range can cause a significant sensor response. Therefore, the pH changes and ionic strength variations should be always monitored in parallel to any other specific detection experiments. We underline the importance of differential measurements for reliable sensing results. If different specific functionalizations are used on one chip, nanowire arrays represent an ideal platform for such multi-analyte detection systems.

6

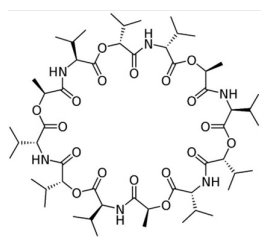
Additional investigations

After the extensive study of the electrolyte background, we can now attempt a selective detection of target species other than protons. In this chapter, we will present some previously unpublished results obtained during this thesis that will be important for future experiments. In particular, we will first show two promising functionalization schemes for the detection of potassium ions. In addition, we will discuss first successful biosensing experiments with a lectin-sugar system.

6.1 Ionophores in a polymer membrane

To demonstrate specific sensing of ions other than protons, several functionalization schemes were tested. To start with, we tried a standard recipe (Fluka, see⁹⁷) based on a polyvinylchloride (PVC) membrane containing a well-known K^+ -selective ionophore valinomycin (left part of Figure 6.1). All components were mixed together and drops of the mixture were placed on two of four nanowire arrays by a syringe (right part of Figure 6.1). After drying at room temperature, measurements in electrolyte solutions were done. Figure 6.2 a shows the measured threshold voltages V_{th} vs. KCl concentration in mol/l for two different nanowires, with and without ionophore. A clear difference between the two nanowires is observed. While the non-covered nanowire exhibits the usual background response, which was carefully studied in the previous chapter, the V_{th} of the coated nanowire shifts

to the opposite direction, i.e. towards more negative potential values. This behavior already indicates adsorption of positively charged species. To remove the background effect, the signal of the reference nanowire (without ionophore) was subtracted from the sensing signal (with K^+ ionophore). The difference ΔV_{th} is plotted in Figure 6.2 b, revealing a clear linear response to K^+ with a negative slope of up to -54 mV/dec . The selectivity of the sensor against other ions was checked in $MgCl_2$ solutions (Figure 6.2 c). Both sensor and reference show very similar background response, and, consequently, the signal difference is nearly zero (Figure 6.2 d), proving high selectivity against Mg^{2+} .



Valinomycin: K^+ ionophore

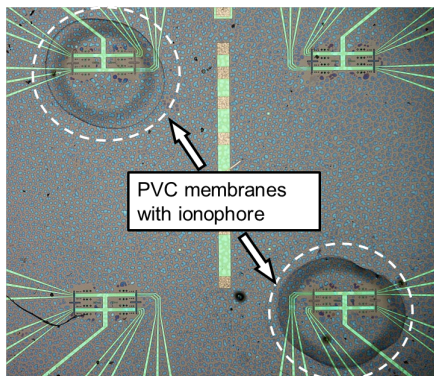


Figure 6.1: Left: Structure of the K^+ -selective ionophore valinomycin. Right: Optical image of a sample after drop deposition of PVC membranes containing valinomycin. Non-coated arrays were used as reference for differential measurements.

6.2 Covalently bound ionophores

Crown ethers are cyclic poly-ethoxy ethers which have the potential to selectively trap metal ions on the basis of their chain length and hence the cavity diameter.⁹⁸ Covalently attached ion traps offer various advantages when compared to membrane embedded ionophores. The risk of desorption of the trapping molecules is reduced and measurements are independent of the diffusion of the analyte in the membrane.

The selected ionophore is supposed to be selective towards K^+ ions. The functionalization procedure is illustrated in the left part of Figure 6.3. The nanowire surface was prepared by silanization of the activated metal oxide surface (Al_2O_3 or HfO_2) with (3-Glycidoxypropyl)triethoxysilane (GOPS)

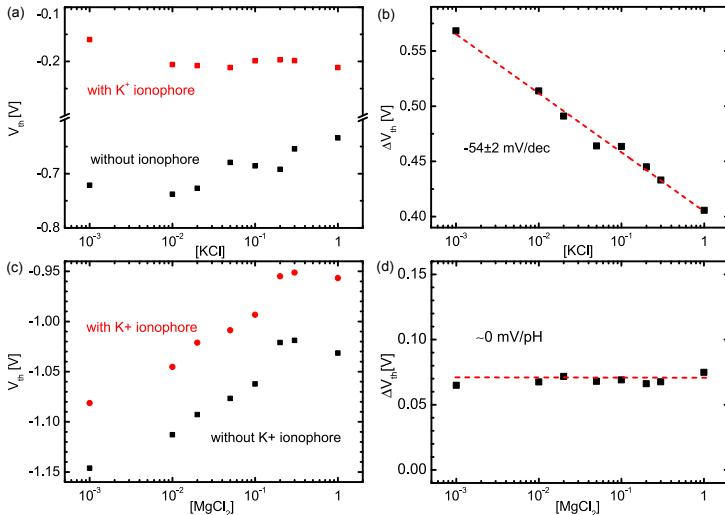


Figure 6.2: (a) Threshold voltage V_{th} versus KCl concentration in deionized water. Without ionophore, the previously described electrolyte background effect occurs (reference). In contrast, V_{th} moves to more negative values with the K^+ -selective ionophore, indicating adsorption of positively charged species (sensor). Subtracting reference from sensor yields the symbols shown in (b). A clear linear response to K^+ is observed with a negative slope of -54 ± 2 mV/dec. (c) To test the selectivity of the ionophore, a measurement in $MgCl_2$ solution was done. Both sensor and reference show the same background response. (d) The differential signal is approximately zero, demonstrating strong selectivity of the sensor against Mg^{2+} .

by vapor-phase deposition (VPD) providing a silane monolayer with epoxy moieties. These epoxy groups then allowed for the convenient attachment of 2-aminomethyl-18-crown-6 (A18C6) by ring opening in aqueous basic conditions. The surface modification was verified by contact angle measurements and X-ray photoelectron spectroscopy (XPS) on Al_2O_3 -coated silicon wafer pieces. The XPS data is shown in the right part of Figure 6.3. Most prominent peaks result from the Al_2O_3 surface (Al 2s and O 1s), however significant amount of nitrogen (N 1s), silicon (Si 2p) and carbon (C 1s) was found as well. This provides evidence for the presence of N-H and Si-O bonds on the surface (highlighted in the left part of the Figure).

The electrical measurements in electrolyte solutions are summarized in Figure 6.4. In part a, the threshold voltage V_{th} is depicted as a function of the electrolyte concentration. To prepare the solutions, either KCl or NaCl was dissolved in deionized water. If the nanowire is functionalized with

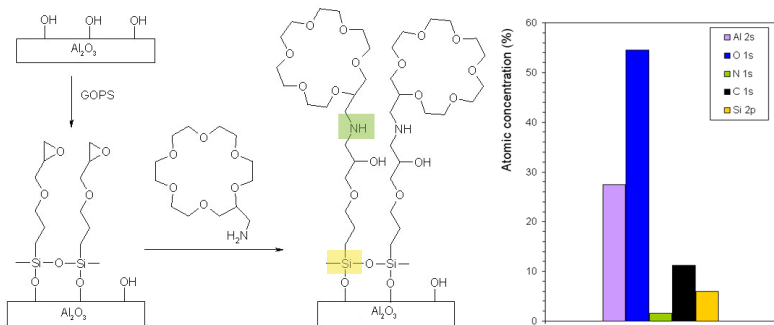


Figure 6.3: Left: The surface functionalization consisted of several steps. First, the oxide was activated by UV/ozone treatment. Then, the surface was silanized in 3-Glycidyloxypropyltrimethoxysilane (GOPS) vapor. In a third step, a K^+ -selective ionophore (2-Aminomethyl-18-crown-6) was attached via amino-epoxide reaction to the immobilized GOPS. The surface modification was verified by contact angle measurements and X-ray photoelectron spectroscopy (XPS). Highlighted parts were resolved by XPS. Right: XPS results from an Al_2O_3 -coated silicon wafer piece after all functionalization steps, showing relative atomic concentrations. Most prominent features are due to the 20 nm thick Al_2O_3 layer (Al 2s and O 1s). In addition, carbon (C 1s), silicon (Si 2p) and nitrogen (N 1s) are present on the surface indicating successful functionalization. Surface modification and characterization were done in collaboration with Jolanta Kurz and Johann Grognum.

the K^+ -selective ionophore, the V_{th} shifts to more negative values with increasing KCl concentration (lower data points), indicating the adsorption of positively charged species. After removing the silane and the ionophore by a UV/ozone treatment, the previously described background effect is completely restored (middle data points). Subtracting the data after cleaning from the functionalized case yields an almost linear sensor response ΔV_{th} to K^+ with a slope of around -40 mV/dec (Figure 6.4 b). To prove the selectivity of the ionophore, a control measurement in NaCl was performed while the sample was still functionalized (upper data points in Figure 6.4 b). No significant difference to the non-functionalized reference was observed. Subtracting reference from the sensor signal results in almost zero response to Na^+ proving the selectivity of the ionophore (Figure 6.4 b).

Recently, the next stage in the development of metal ion sensing using NW has been achieved. In order to improve the quality and reliability of the measurements using on-chip referencing represents an ideal solution. It allows for simultaneous measurements on a single chip of both reference and sensing NW thus reducing variations in conditions, independent of absolute potential in liquids. This could be performed by covering the nanowire with

a PDMS based microfluidics after silanization in VPD conditions. With a single channel running over 2 arrays of nanowires (out of 4) we were able to selectively functionalize these arrays with 18-crown-6 ethers by flowing the A18C6 solution with a syringe pump in similar conditions as above described. The performance obtained was comparable to the previous experiments. A detailed functionalization protocol is provided in Appendix C.

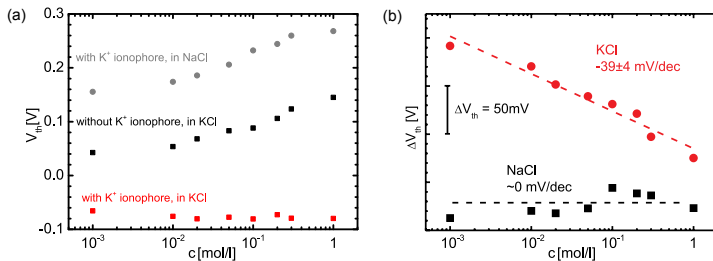


Figure 6.4: (a) Threshold voltage V_{th} versus electrolyte concentration. When the sample is covered with a K^+ -selective ionophore, V_{th} shifts to more negative values with increasing KCl concentration (lower data points). In contrast, V_{th} of the same ionophore-covered sample increases with NaCl concentration (upper data points), behaving similar to the uncoated reference (middle data points). (b) Differential signal ΔV_{th} (sensor minus uncoated reference from part a) as a function of KCl and NaCl concentration. The sensor shows linear response of about -40 mV/dec to K^+ and almost no response to Na^+ .

6.3 Sensing lectin-sugar interactions

Lectins are highly specific sugar-binding proteins. Lectin/carbohydrate interactions play a key role in many biological processes, for example, during the initial phase of the bacterial urinary tract infection. The bacterium uses the lectin FimH, located at the tip of its pili, to attach to the epithelial cells of the host. The ligands on the host cell surface are carbohydrate structures, mostly oligomannosides. The contact between bacterium and host cell precedes the infectious process. As a long-term goal, nanowire-based sensors could be used to screen biological liquids to identify components with high adhesion affinity to lectins. These components would become the starting point for the development of new anti-infective drugs.

To gain first insights into this test system, a ligand with a strong binding affinity to FimH was chosen, n-heptyl-mannose. The affinity was determined by surface plasmon resonance to be in the nanomolar range (~ 50 nM, measurements performed in the group of Prof. Beat Ernst, University of Basel).

Prior to nanowire sensing experiments, the surface modification scheme for the ligand attachment on an oxide surface was developed by Jolanta Kurz (FHNW, Muttentz). The interaction between the lectin and the immobilized ligand was studied by quartz crystal microbalance (QCM). After successful QCM tests, a nanowire sample was first silanized by vapor phase deposition of Aminopropyltrimethylmethoxysilane (APTES 1) and then functionalized with n-heptyl-mannose (Figure 6.5 a). For control purposes, a different sample was passivated by a non-binding ligand without a sugar moiety (8-OH heptanoic acid, Figure 6.5 b). Ligands and lectins were provided by Beat Ernst's group, the functionalization was done in cooperation with Jolanta Kurz, Arjan Odedra and Giulio Navarra. In later experiments (not shown), 2 of 4 arrays (pixels) of each sample were selectively functionalized using PDMS microfluidics, to have the active and the control nanowires measured simultaneously on the same chip. The details of the surface modification are given in Appendix D.

Preliminary sensing results are plotted in Figure 6.5 c and d. In part c, the signal change of the activated nanowire ΔI is shown as a function of time. A straight line has been subtracted from the measured current to make the comparison between different wires easier. First, the sample is brought in contact with a HEPES buffer solution (≈ 150 mM, $\text{pH} = 7.4$). The working point of the nanowire FET is fixed by the back-gate V_{bg} and the liquid gate voltage V_{lg} . After a stable baseline has been obtained, the solution is exchanged by the same HEPES buffer, this time containing $2 \mu\text{g/ml}$ or ≈ 100 nM of lectin. A clear current increase is observed. The current increases even further upon addition of a 5 times higher lectin concentration. Washing with plain buffer solution afterwards does not change the signal level any more (not shown). In contrast to the active nanowire, no significant signal change occurs in the case of the passivated nanowire (part d). The observed current rise (part c) implies that negatively charged species attached to the sensor surface. This seems to be plausible because the isoelectric point of the FimH protein is around $\text{pI} \approx 6.7$. Therefore, the lectin is negatively charged at $\text{pH} = 7.4 > \text{pI}$, which results in additional negative gating of the p-doped nanowire and a current increase. These results have been recently reproduced with different samples. Currently running studies also focus on improving the signal intensity. In particular, this includes measuring at higher pH values to increase the charge of the lectin, lowering the electrolyte concentration to reduce charge screening effects, and optimizing the surface chemistry. More measurements are needed for a detailed quantitative analysis of the kinetics and affinities of the lectin/sugar binding as well as their comparison with surface plasmon resonance data.

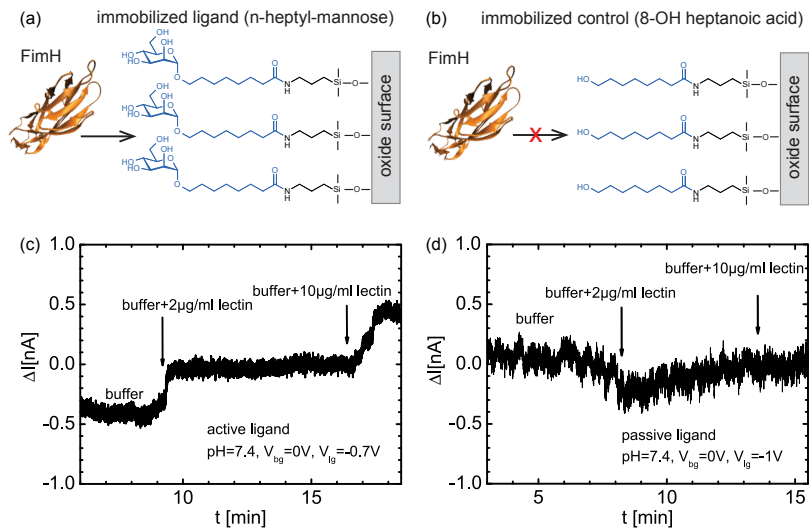


Figure 6.5: The silanized oxide surface of nanowire samples and QCM test devices was either functionalized by an active ligand, n-heptyl-mannose (a) or passivated by a non-binding control, 8-OH heptanoic acid (b). Preliminary FimH sensing results from the active nanowire (c) and from the passivated negative control (d). (c) The change in source-drain current ΔI vs. time after subtracting a straight line. The current increases upon addition of lectin to the buffer solution, suggesting the attachment of negatively charged species. (d) In contrast, no significant signal change occurs for the control sample.

Conclusions and Outlook

In this dissertation, we have established a reliable sensing platform based on arrays of silicon nanowire field-effect transistors. One of the first milestones has been the stable operation in electrolyte environment. This is achieved by a drastic reduction of leakage currents using atomic layer deposition (ALD) of high-quality oxide interfaces.¹³ In Chapter 2, we show that Si NW are excellent pH sensors with nearly ideal Nernstian response of 58.2 mV/dec at 20°C. This is also attributed to the high quality of the active gate dielectric (high-k Al_2O_3 or HfO_2). Because the pH sensitivity is a property of the oxide/electrolyte interface, no influence of the nanowire size on the pH response is found.⁴³

Chapter 3 focuses on the low-frequency noise measurements and explores the ultimate detection limits set by the noise of the transistor.^{45,99} The deduced gate-referred threshold voltage noise δV_{th} is the true figure of merit in such transistor-based sensors. We demonstrate that δV_{th} is constant over the full operation range of the transistor, as long as the intrinsic nanowire resistance dominates and the contact resistance can be neglected. Both linear and subthreshold regime can be used for equally sensitive pH measurements with a detection limit of ~ 200 ppm of a full Nernstian pH shift (1 Hz bandwidth at 10 Hz, 1 μm wide NW).

Even though great progress has been achieved in pH sensing, it has turned out to be much harder to realize a true reference electrode, which – while sensing the electrostatic potential – does not respond to the proton concentration. In Chapter 4, we demonstrate a highly effective reference sensor, whose proton sensitivity is suppressed by as much as two orders of magnitude. To do so, the Al_2O_3 surface of a nanowire FET is passivated with a self-assembled monolayer of silanes with a long alkyl chain (C 18). We find that a full passivation can be achieved only after several days of self-assembly. In addition, we determine the number of proton-binding surface sites as a function of silanization time by quantitatively comparing the experimental data with the theoretical site-binding model. Furthermore, we find that a partially passivated surface can sense small changes in the number of active sites caused by the adsorption of *uncharged* species. A detection limit for this type of application is estimated. This result might extend the application field of ion-sensitive FETs to the detection of neutral species.

Understanding the electrolyte background is a basic prerequisite for any further biochemical sensing. In Chapter 5, we study the sensor response to changes in KCl concentration at several constant pH values. A significant signal change is only observed at high ionic strengths > 10 mM. Our measurements suggest that anions (Cl^-) rather than cations (K^+) adsorb on the surface, independent of the pH value. By comparing the data to three well-established models, we find that none of those can completely explain the results. We propose a new adsorption model instead which gives excellent agreement with the data. According to our model, the chloride ions directly interact with the hydroxyl surface groups and replace previously attached protons.

In Chapter 6 we report our efforts to selectively sense targets other than protons. Using ionophores embedded in PVC membranes, we demonstrate selective detection of potassium ions in a differential set-up. We also show that a different functionalization scheme, based on covalent silane chemistry, can be equally effective. Moreover, first successful and reproducible biosensing measurements of a specific sugar-lectin interaction are presented.

Based on the promising biosensing results, future experiments will aim at a more systematic study of sugar-lectin interactions to quantify the affinities and kinetics of this particular system. Further biosensing measurements could also include indirect detection schemes, for example, if a biological process results in a local pH change close to the sensor surface, such a pH change might be detected. This approach could increase the signal intensity. Ultimately, a high-throughput tool based on nanowire arrays for disease diagnostics or drug discovery is envisioned.

Concerning the chemical sensing, further experiments are planned to extend the existing covalent functionalization schemes to different target ions, such as calcium, magnesium or certain heavy metal ions. To be even more flexible in terms of functionalization, currently running experiments focus on the coating of nanowires with lithography-made thin gold films or stamped gold nanoparticles. This gives access to the established thiol-based surface chemistry. First successful measurements have been already performed using gold-coated nanowires functionalized with sodium-selective ionophores. In the case of nanoparticles, a hybrid sensing system that combines the advantages of optical and electrical read-out methods is within reach. Together with the ongoing work towards the integration of the sensor and the read-out electronics on one chip, the mentioned functionalization methods will enable a highly efficient multi-analyte detection system with a commercial potential, for example in the area of water quality monitoring.

Bibliography

- [1] P. Bergveld. Thirty years of isfetology: What happened in the past 30 years and what may happen in the next 30 years. *Sensors and Actuators B*, 1:1, 2003.
- [2] S. J. Tans, A. R. M. Verschueren, and C. Dekker. Room-temperature transistor based on a single carbon nanotube. *Nature*, 393:49, 1998.
- [3] J. Kong, N. Franklin, C. Zhou, M. Chapline, S. Peng, K. Cho, and H. Dai. Nanotube molecular wires as chemical sensors. *Science*, 287:622, 2000.
- [4] P. Collins, K. Bradley M. Ishigami, and A. Zettl. Extreme oxygene sensitivity of electronic properties of carbon nanotubes. *Science*, 287:1801, 2000.
- [5] M. Krüger, M.R. Buitelaar, T. Nussbaumer, and C. Schönberger. Electrochemical carbon nanotube field-effect transistors. *Appl. Phys. Lett.*, 78:1291, 2001.
- [6] P. Ang, W. Chen, A. Wee, and K. Ping. Solution-gated epitaxial graphene as pH sensor. *J. Am. Chem. Soc.*, 130:14392–14393, 2008.
- [7] Y. Ohno, K. Maehashi, Y. Yamashiro, and K. Matsumoto. Electrolyte-gated graphene field-effect transistors for detecting pH and protein adsorption. *Nano Lett.*, 9:3318–3322, 2009.
- [8] Z. Cheng, Q. Li, Z. Li, Q. Zhou, , and Y. Fang. Suspended graphene sensors with improved signal and reduced noise. *Nano Lett.*, 10:1864, 2010.
- [9] W. Fu, C. Nef, O. Knopfmacher, A. Tarasov, M. Weiss, M. Calame, and C. Schönberger. Graphene transistors are insensitive to pH changes in solution. *Nano Lett.*, 11:3597–3600, 2011.
- [10] X. Duan, Y. Huang, Y. Cui, J. Wang, and C. Lieber. Indium phosphide nanowires as building blocks for nanoscale electronic and optoelectronic devices. *Nature*, 409:66, 2001.

- [11] Y.Q. Cui, Wei Q., H.K. Park, and C.M. Lieber. Nanowire nanosensors for highly sensitive and selective detection of biological and chemical species. *Science*, 293:1289–1292, 2001.
- [12] E. Stern, J. F. Klemic, D. A. Routenberg, P. N. Wyrembak, D. B. Turner-Evans, A. D. Hamilton, D. A. LaVan, T.M. Fahmy, and M. Reed. Label-free immunodetection with CMOS-compatible semiconductor nanowires. *Nature*, 445:519, 2007.
- [13] O. Knopfmacher, A. Tarasov, W. Fu, M. Wipf, B. Niesen, M. Calame, and C. Schönenberger. Nernst limit in dual-gated Si-nanowire FET sensors. *Nano Lett.*, 10:2268, 2010.
- [14] S. Chen, J.G. Bomer, E.T. Carlen, and A. van den Berg. Al₂O₃/silicon nanoISFET with near ideal Nernstian response. *Nano Lett.*, 11(6):2334, 2011.
- [15] L. Luo, J. Jie, W. Zhang, Z. He, J. Wang, G. Yuan, W. Zhang, L.C.M. Wu, and S-T. Lee. Silicon nanowire sensors for Hg²⁺ and Cd²⁺ ions. *Appl. Phys. Lett.*, 94:193101, 2009.
- [16] X. Bi, A. Argawal, and K.L. Yang. Oligopeptide-modified silicon nanowire arrays as multichannel metal ion sensors. *Biosens. Bioelectron.*, 24:3248, 2009.
- [17] G. Zheng, F. Patolsky, Y. Cui, W. Wang, and C. Lieber. Multiplexed electrical detection of cancer markers with nanowiresensor arrays. *Nat. Biotechnol.*, 23:1294, 2005.
- [18] Y.L. Bunimovich, Y.S. Shin, W-S Yeo, Amori M., G. Kwong, and J.R. Heath. Quantitative real-time measurements of DNA hybridization with alkylated nonoxidized silicon nanowires in electrolyte solution. *J. Am. Chem. Soc.*, 128:16323–16331, 2006.
- [19] N. Elfström, A. E. Karlström, and J. Linnros. Silicon nanoribbons for electrical detection of biomolecules. *Nano Lett.*, 8:945–949, 2008.
- [20] E. Stern, A. Vacic, N. K. Rajan, J. M. Criscione, J. Park, B. R. Ilic, D. J. Mooney, M. A. Reed, and T. M. Fahmy. Label-free biomarker detection from whole blood. *Nat. Nanotechnol.*, 5:138–142, 2010.
- [21] D. R. Kim, C. H. Lee, and X. Zheng. Probing flow velocity with silicon nanowire sensors. *Nano Lett.*, 9:1984–1988, 2009.

- [22] Y. Engel, R. Elnathan, A. Pevzner, G. Davidi, E. Flaxer, and F. Patolsky. Supersensitive detection of explosives by silicon nanowire arrays. *Angew. Chem., Int. Ed.*, 49:6830–6835, 2010.
- [23] G. Gruner. Carbon nanotube transistors for biosensing applications. *Anal. Bioanal. Chem.*, 384:322–335, 2006.
- [24] F. Patolsky, G. Zheng, O. Hayden, M. Lakadamyali, X. Zhuang, and C. Lieber. Electrical detection of single viruses. *Proc. Nat. Acad. Sci.*, 101:14017–14022, 2004.
- [25] B. Tian, T. Cohen-Karni, Q. Qing, X. Duan, P. Xie, and C. M. Lieber. Three-dimensional, flexible nanoscale field-effect transistors as localized bioprobes. *Science*, 329:830–834, 2010.
- [26] X. Duan, R. Gao, P. Xie, T. Cohen-Karni, Q. Qing, H. S. Choe, B. Tian, X. Jiang, and C. M. Lieber. Intracellular recordings of action potentials by an extracellular nanoscale field-effect transistor. *Nat. Nanotechnol.*, 7:174–179, 2012.
- [27] N. Elfström, R. Juhasz, I. Sychugov, T. Engfeldt, A. Eriksson, and J. Linnros. Surface charge sensitivity of silicon nanowires: Size dependence. *Nano Lett.*, 7:2608, 2007.
- [28] F. Patolsky, B. Timko, G. Yu, Y. Fang, A. Greytank, G. Zheng, and C. Lieber. Detection, stimulation, and inhibition of neuronal signals with high-density nanowire transistor arrays. *Science*, 313:1100–1104, 2006.
- [29] I. Park, Z. Li, A.P. Pisano, and R.S. Williams. Top-down fabricated silicon nanowire sensor for real-time chemical detection. *Nanotechnology*, 21:015501, 2009.
- [30] Nobel Media AB. The first transistor, available from: <http://www.nobelprize.org/educational/physics/transistor/function/firsttransistor.html>, 2012.
- [31] Intel Corporation. Der Transistor wird 60 Jahre alt, 2007.
- [32] S.M. Sze and K.K. Ng. *Physics of Semiconductor Devices*. John Wiley & Sons, 2007.
- [33] Y.P. Tsividis. *Operation and Modeling of the MOS Transistor*. McGraw-Hill, New-York, 1987.

- [34] P. Bergveld. Development of an ion-sensitive solid-state device for neurophysiological measurements. *IEEE Trans Biomed Eng.*, 17:70, 1970.
- [35] D. E. Yates, S. Levine, and T. W. Healy. Site-binding model of the electrical double layer at the oxide/water interface. *J. Chem. Soc., Faraday Trans.*, 70:1807–1818, 1974.
- [36] T. W. Healy and L. R. White. Ionizable surface group models of aqueous interfaces. *Adv. Colloid Interface Sci.*, 9:303–345, 1978.
- [37] L. Bousse, N. F. de Rooij, and P. Bergveld. Operation of chemically sensitive field-effect sensors as a function of the insulator-electrolyte interface. *IEEE Trans. Electron Devices*, 30:1263–1270, 1983.
- [38] A. van den Berg, P. Bergveld, D. N. Reinhoudt, and E. J. R. Sudhölter. Sensitivity control of ISFETs by chemical surface modification. *Sens. Actuators*, 8:129–148, 1985.
- [39] R. E. G. van Hal, J. C. T. Eijkel, and P. Bergveld. A general model to describe the electrostatic potential at electrolyte oxide interfaces. *Adv. Colloid Interface Sci.*, 69:31–62, 1996.
- [40] Oren Knopfmacher. *Sensing with Silicon Nanowire Field-Effect Transistors*. PhD thesis, University of Basel, 2011.
- [41] O. Knopfmacher, A. Tarasov, M. Wipf, W. Fu, M. Calame, and C. Schönenberger. Silicon-based ion-sensitive field-effect transistor shows negligible dependence on salt concentration at constant pH. *ChemPhysChem*, 13:1157–1160, 2012.
- [42] A. Tarasov, M. Wipf, Bedner K., J. Kurz, W. Fu, V. A. Guzenko, O. Knopfmacher, R. L. Stoop, M. Calame, and C. Schönenberger. True reference electrode realized with silicon nanowires. *Langmuir*, 28:9899–9905, 2012.
- [43] K. Bedner, V. A. Guzenko, A. Tarasov, M. Wipf, R. L. Stoop, D. Just, S. Rigante, O. Knopfmacher, W. Fu, R. A. Minamisawa, C. David, M. Calame, J. Gobrecht, and C. Schönenberger. pH-response of silicon nanowire sensors: Impact of the nanowire width and the gate oxide. *submitted to Nanotechnology*, 2012.
- [44] O. Knopfmacher, D. Keller, M. Calame, and C. Schönenberger. Dual gated silicon nanowire field effect transistors. *Procedia Chemistry*, 1: 678–681, 2009.

- [45] A. Tarasov, W. Fu, O. Knopfmacher, J. Brunner, M. Calame, and C. Schönenberger. Signal-to-noise ratio in dual-gated silicon nanoribbon field-effect sensors. *Appl. Phys. Lett.*, 98:012114, 2011.
- [46] J. Robertson. High dielectric constant gate oxides for metal oxide Si transistors. *Rep. Prog. Phys.*, 69:327–396, 2006.
- [47] S. Zafar, C. D’Emic, A. Afzali, B. Fletcher, Y. Zhu, and T. Ning. Optimization of pH sensing using silicon nanowire field effect transistors with HfO_2 as the sensing surface. *Nanotechnology*, 22:405501, 2011.
- [48] J.-H. Ahn, S.-J. Choi, J.-W. Han, T. J. Park, S. Y. Lee, and Y.-K. Choi. Investigation of size dependence on sensitivity for nanowire FET biosensors. *IEEE Trans. Nanotechnol.*, 10:1405–1411, 2011.
- [49] X. Duan, Y. Li, N. K. Rajan, D. A. Routenberg, Y. Modis, and M. A. Reed. Quantification of the affinities and kinetics of protein interactions using silicon nanowire biosensors. *Nat. Nanotechnol.*, DOI: 10.1038/nnano.2012.82, 2012.
- [50] I. Heller, J. Männik, S. Lemay, and C. Dekker. Optimizing the signal-to-noise ratio for biosensing with carbon nanotube transistors. *Nano Lett.*, 9:377, 2009.
- [51] X.A. Gao, G. Zheng, and C. Lieber. Subthreshold regime has the optimal sensitivity for nanowire FET biosensors. *Nano Lett.*, 10:547, 2010.
- [52] N. Clement, K. Nishiguchi, J.F. Dufreche, D. Guerin, A. Fujiwara, and D. Vuillaume. A silicon nanowire ion-sensitive field-effect transistor with elementary charge sensitivity. *Appl. Phys. Lett.*, 98:014104, 2011.
- [53] N. K. Rajan, D. A. Routenberg, J. Chen, and M. Reed. $1/f$ noise of silicon nanowire bioFETs. *IEEE Electr. Device L.*, 31:615, 2010.
- [54] N. K. Rajan, D. A. Routenberg, and M. Reed. Optimal signal-to-noise ratio for silicon nanowire biochemical sensors. *Appl. Phys. Lett.*, 98: 264107, 2011.
- [55] F. N. Hooge, T. G. M. Kleinpenning, and L. K. J. Vandamme. Experimental studies on $1/f$ noise. *Rep. Prog. Phys.*, 44:479, 1981.
- [56] F. N. Hooge. $1/f$ noise is no surface effect. *Phys. Lett. A*, 29:139, 1969.
- [57] C. G. Jakobson and Y. Nemirovsky. $1/f$ noise in ion sensitive field effect transistors from subthreshold to saturation. *IEEE Trans. Electron Devices*, 46:259–261, 1999.

- [58] E. Sudhölter, L. de Smet, M. Mescher, and D. Ullien. Organic surface modification of silicon nanowire-based sensor devices, nanowires – implementations and applications, Hashim A.(Editor). ISBN: 978-953-307-318-7, InTech, 2011. Available from: <http://www.intechopen.com/articles/show/title/organic-surface-modification-of-silicon-nanowire-based-sensor-devices>.
- [59] H. Nakajima, M. Esashi, and T. Matsuo. The cation concentration response of polymer gate ISFET. *J. Electrochem. Soc.*, 129:141–143, 1982.
- [60] P. Bergveld, A. van den Berg, P. D. van der Wal, M. Skowronska-Ptasinska, E. J. R. Sudhölter, and D. N. Reinhoudt. How electrical and chemical requirements for REFETs may coincide. *Sens. Actuators*, 18: 309–327, 1989.
- [61] H. Perrot, N. Jaffrezic-Renault, N. F. de Rooij, and H. H. van den Vlekkert. Ionic detection using differential measurement between an ion-sensitive FET and a reference FET. *Sens. Actuators*, 20:293–299, 1989.
- [62] P. Battaillard, P. Clechet, N. Jaffrezic-Renault, X. G. Kong, and C. Martelet. The preparation of chem-FET selective gates by thin silica layer grafting and their behaviour. *Sens. Actuators*, 12:245–254, 1987.
- [63] B. Dorvel, B. Reddy, I. Block, P. Mathias, S. E. Claire, B. Cunningham, D. E. Bergstrom, and R. Bashir. Vapor-phase deposition of monofunctional alkoxy silanes for sub-nanometer-level biointerfacing on silicon oxide surfaces. *Adv. Funct. Mater.*, 20:87–95, 2010.
- [64] C. D. Fung, P. W. Cheung, and W. H. Ko. A generalized theory of an electrolyte-insulator-semiconductor field-effect transistor. *IEEE Trans. Electron Devices*, 33:8–18, 1986.
- [65] D. Janssen, R. de Palma, S. Verlaak, P. Heremans, and W. Dehaen. Static solvent contact angle measurements, surface free energy and wettability determination of various self-assembled monolayers on silicon dioxide. *Thin Solid Films*, 515:1433–1438, 2006.
- [66] Gelest. Hydrophobicity, hydrophilicity and silane surface modification. available from: <http://www.gelest.com/goods/pdf/hydrophobicity.pdf>, 2012.
- [67] power = 30 W pressure = 250 mTorr Following parameters for the oxygen plasma cleaning were used: time = 30 s.

- [68] The actual measured quantity is the threshold voltage V_{th} . assuming $PZC = 7$, we subtract all V_{th} values from the value at $pH = 7$, that is $V_{th}(PZC)$. the resulting ΔV_{th} is zero at the PZC, positive at pH values $< PZC$ and negative at $pH > PZC$. this makes ΔV_{th} more meaningful than V_{th} .
- [69] J. C. van Kerkhof, J. C. T. Eijkel, and P. Bergveld. ISFET responses on a stepwise change in electrolyte concentration at constant pH. *Sens. Actuators B*, 18-19:56–59, 1994.
- [70] If the value of C_{dl} was different, e.g. two times smaller, it would be compensated in the fits by a two times lower $N_s \propto C_s$, keeping the (important) ratio of C_{dl}/C_s constant, see equation 4.9. the shape or the quality of the fits would not change at all.
- [71] A model with a n_s value below 10^{12} cm^{-2} is not in contradiction with the experiment, but we have chosen a rather conservative upper limit.
- [72] A. Tarasov, M. Wipf, R. L. Stoop, K. Bedner, W. Fu, V. A. Guzenko, O. Knopfmacher, M. Calame, and C. Schönenberger. Understanding the electrolyte background for biochemical sensing with ion-sensitive field-effect transistors. *submitted to ACS Nano*, 2012.
- [73] H. J. Modi and D. W. Fuerstenau. Streaming potential studies on corundum in aqueous solutions of inorganic electrolytes. *J. Phys. Chem.*, 61: 640–643, 1957.
- [74] R. J. Hunter and H. J. L. Wright. The dependence of electrokinetic potential on concentration of electrolyte. *J. Colloid Interface Sci.*, 37: 564–580, 1971.
- [75] C.-P. Huang and W. Stumm. Specific adsorption of cations on hydrous $\gamma\text{-Al}_2\text{O}_3$. *J. Colloid Interface Sci.*, 43:409–420, 1973.
- [76] R. Sprycha. Electrical double layer at alumina/electrolyte interface. *J. Colloid Interface Sci.*, 127:1–11, 1989.
- [77] S. B. Johnson, P. J. Scales, and T. W. Healy. The binding of monovalent electrolyte ions on α -alumina. I. electroacoustic studies at high electrolyte concentrations. *Langmuir*, 15:2836–2843, 1999.
- [78] M. Kosmulski. Confirmation of the differentiating effect of small cations in the shift of the isoelectric point of oxides at high ionic strengths. *Langmuir*, 18:785–787, 2002.

- [79] R. J. Hunter. *Zeta Potential in Colloid Science: Principles and Applications*. 2nd ed.; Academic Press: London, 1988.
- [80] M. Kosmulski. Compilation of PZC and IEP of sparingly soluble metal oxides and hydroxides from literature. *Adv. Colloid Interface Sci.*, 152: 14–25, 2009.
- [81] J. A. Davis, R. O. James, and J. O. Leckie. Surface ionization and complexation at the oxide/water interface I. computation of electrical double layer properties in simple electrolytes. *J. Colloid Interface Sci.*, 63:480–499, 1978.
- [82] F. G. K. Baucke. Fundamental and applied electrochemistry at an industrial glass laboratory – an overview. *J. Solid State Electrochem.*, 15:23–46, 2011.
- [83] A. A. Belyustin. The centenary of glass electrode: from Max Cremer to F. G. K. Baucke. *J. Solid State Electrochem.*, 15:47–65, 2011.
- [84] P. Scholz. Nikolsky's ion exchange theory versus Baucke's dissociation mechanism of the glass electrode. *J. Solid State Electrochem.*, 15:23–46, 2011.
- [85] P. Bergveld. Development, operation, and application of the ion-sensitive field-effect transistor as a tool for electrophysiology. *IEEE Trans. Biomed. Eng.*, BME-19:342–351, 1972.
- [86] D. Sobczynska and W. Torbicz. ZrO₂ gate pH-sensitive field effect transistor. *Sens. Actuators*, 6:93–105, 1984.
- [87] R. E. G. van Hal, J. C. T. Eijkel, and P. Bergveld. A novel description of ISFET sensitivity with the buffer capacity and double-layer capacitance as key parameters. *Sens. Actuators B*, 24-25:201–205, 1995.
- [88] M. Zacharias, N. S. Ramgir, and Y. Yang. Nanowire-based sensors. *Small*, 6:1705–1722, 2010.
- [89] A. Kolmakov and M. Moskovits. Chemical sensing and catalysis by one-dimensional metal-oxide nanostructures. *Annu. Rev. Mater. Res.*, 34:151–180, 2004.
- [90] C.M. Lieber, F. Patolsky, and G. F. Zheng. Nanowire-based biosensors. *Anal. Chem.*, 78:4260–4269, 2006.

- [91] M.G. Nikolaides, S. Rauschenbach, S. Lubner, K. Bucholz, M. Tornow, G. Abstreiter, and A.R. Bausch. Silicon-on-insulator based thin-film resistor for chemical and biological sensor applications. *ChemPhysChem*, 4:1104, 2003.
- [92] T.-F. Lu, C.-M. Yang, J.-C. Wang, K.-I. Ho, C.-H. Chin, D.G. Pijanowska, B. Jaroszewicz, and C.-S. Lai. Characterization of K^+ and Na^+ -sensitive membrane fabricated by CF_4 plasma treatment on hafnium oxide thin films on ISFET. *J. Electrochem. Soc.*, 158:J91–J95, 2011.
- [93] C. Bretti, C. Foti, N. Porcino, and S. Sammartano. SIT parameters for 1:1 electrolytes and correlation with Pitzer coefficients. *J. Solution. Chem.*, 35:1401–1415, 2006.
- [94] M. Kosmulski. Attempt to determine pristine points of zero charge of Nb_2O_5 , Ta_2O_5 , and HfO_2 . *Langmuir*, 13:6315–6320, 1997.
- [95] L. J. Criscenti, R. T. Cygan, A. S. Kooser, and H. K. Moffat. Water and halide adsorption to corrosion surfaces: Molecular simulations of atmospheric interactions with aluminum oxyhydroxide and gold. *Chem. Mater.*, 20:4682–4693, 2008.
- [96] R. Taylor and Kennard O. Crystallographic evidence for the existence of C-H \cdots O, C-H \cdots N, and C-H \cdots Cl hydrogen bonds. *J. Am. Chem. Soc.*, 104:5063–5070, 1982.
- [97] Sigma-Aldrich. Protocol for potassium ionophores available from: http://www.sigmaaldrich.com/etc/medialib/docs/sigma/instructions/k_potassium.par.0001.file.tmp/k_potassium.pdf.
- [98] J. W. Steed and J. L. Atwood. *Supramolecular chemistry*. John Wiley & Sons, 2009.
- [99] K. Bedner, V. A. Guzenko, A. Tarasov, M. Wipf, R. L. Stoop, J. Brunner, W. Fu, R. A. Minamisawa, C. David, M. Calame, J. Gobrecht, and C. Schönenberger. Scaling of noise limitations in silicon nanowire charge sensors. *submitted*, 2012.

Appendix A: Device fabrication protocol 1

This protocol is taken from the PhD thesis of O. Knopfmacher.⁴⁰

- **SOI wafer characteristics**

<i>Supplier</i>	SIMGUI Technology
<i>Orientation</i>	(100)
<i>Dopant</i>	p, Boron
<i>Resistivity</i>	10-20 Ωm
<i>Device layer thickness</i>	100 nm
<i>BOX layer thickness</i>	150 nm
<i>Substrate thickness</i>	525 μm

- **Cleaving**

<i>Alignment</i>	in $\langle 110 \rangle$ direction
<i>Cut</i>	Scratch with diamond scratcher; cleave
<i>Protection</i>	Do not scratch TOX layer

- **Cleaning procedure**

1. Sonicate in acetone (10 min)
2. Sonicate in 2-propanol (10 min) then dry
3. UV ozone cleaning for 10 minutes (model 42, Jelight Company)

- **UV lithography process**

1. Place wafer onto the spinner
2. Cover wafer with ma-N 415 (Micro Resist, diluted 6:1, 70% Anisole and 30% 2-methoxy-1-methylmethyl-acetate)
3. Spin to obtain 800 nm film (6000 rpm, time= 45 s, ramp= 4 s)
4. Bake out on hotplate (95°C for 90 seconds)
5. Place wafer into mask aligner (MJB-4, Süss Microtec)
6. Align chromium mask in $\langle 110 \rangle$ direction of the wafer (mask obtained from Delta Mask or EPFL)

7. Expose:

<i>Newton rings</i>	broaden and homogeneous distributed
<i>WEC pressure</i>	1.2 – 1.4 bar
<i>Hard contact time</i>	6 s
<i>Expose</i>	10 s
8. Develop for ~ 100 s in maD-323 developer
9. Evaporation of chromium in Balzers-Pfeiffer PLS 500:

<i>Sample temperature</i>	0°C
<i>Base pressure</i>	10^{-7} mbar
<i>Rate</i>	1-2 Å/s
<i>Thickness</i>	60 nm
10. Lift-off in warm acetone
11. Rinse in 2-propanol and dry

• **E-beam process**

1. Place wafer onto the spinner
2. Cover wafer with ma-N 415
3. Spin film (4000 rpm, time= 45 s, ramp= 4 s)
4. Bake out on hotplate (95°C for 90 s)
5. Place wafer into mask aligner
6. Align chromium mask in $\langle 110 \rangle$ direction of the wafer
7. Expose:

<i>WEC pressure</i>	1.2 – 1.4 bar
<i>Hard contact time</i>	6 s
<i>Expose</i>	13 s
8. Develop for ~ 45 s in maD-323 developer
9. Evaporation of chromium:

<i>Sample temperature</i>	0°C
<i>Base pressure</i>	10^{-7} mbar
<i>Rate</i>	1-2 Å/s
<i>Thickness</i>	60 nm
10. Lift-off in warm acetone
11. Rinse in 2-propanol and dry
12. Place wafer onto the spinner

13. Cover wafer with PMMA (AR-P 671.09 950K from ALLRESIST, diluted)
14. Spin to obtain 350 nm film (4000rpm, time= 40 s, ramp= 4 s)
15. Bake out in oven (180°C for 30 min)
16. Write nanowire and small contact leads with SEM (Jeol, Leo or Zeiss Supra 40)
17. Develop for 90 s in 4-methyl-2-pentanone (25 %), 2-propanol (75 %)
18. Rinse for 90 s in 2-propanol and dry
19. Evaporation of chromium:

<i>Sample temperature</i>	0°C
<i>Base pressure</i>	10^{-7} mbar
<i>Rate</i>	1-2 Å/s
<i>Thickness</i>	80 nm
20. Lift-off in warm acetone
21. Rinse in 2-propanol and dry

- **TOX layer etching**

1. Place wafer in plasma etcher (Plasmalab^{80Plus}, Oxford)
2. 2 min O₂ plasma (recipe for PMMA strip):

<i>gas</i>	O ₂
<i>flow</i>	16
<i>pressure 1</i>	25 mTorr look up name
<i>pressure 2</i>	$5 \cdot 10^{-5}$ bar look up name
<i>RF power</i>	100 W

3. 2 min 30 s CHF₃ plasma:

<i>gas</i>	CHF ₃
<i>flow</i>	40
<i>pressure 1</i>	25 mTorr look up name
<i>pressure 2</i>	$5 \cdot 10^{-5}$ bar look up name
<i>RF power</i>	100 W

4. 2 min O₂ plasma (recipe for PMMA strip):

<i>gas</i>	O ₂
<i>flow</i>	16
<i>pressure 1</i>	25 mTorr look up name
<i>pressure 2</i>	$5 \cdot 10^{-5}$ bar look up name
<i>RF power</i>	100 W

- **Chromium etching**

1. Place wafer into a beaker with etch solution (NaOH, KMNO_4 and deionized water, ratio 3:2:12)
2. Shake for 10 min
3. Place wafer in beaker with deionized water
4. Shake for 2 min
5. Wash twice more in deionized water
6. Rinse in 2-propanol and dry

- **Native oxide etching**

1. Dip wafer for 1 min deionized water to wet surface
2. Dip wafer for short time ($\sim 5 - 20$ s; depends on TOX thickness) in buffered hydrofluoric acid (1:20)
3. Wash three times in deionized water
4. Wash in 2-propanol

- **Device layer etching**

1. Place wafer into beaker with tetramethylammoniumhydroxide (25% in water) and 10% 2-propanol

Temperature 45°C

Stirring Controlled vigorous stirring

Etching time 10-15 min; depends on device layer thickness

2. Wash three times in deionized water to stop etching
3. Wash in 2-propanol and dry

- **Contacts**

1. Place wafer onto the spinner
2. Cover wafer with hexamethyldisilazan (HMDS)
3. Spin film (4000 rpm, time= 45 s, ramp= 4 s)
4. Cover wafer with ma-N 415
5. Spin film (4000 rpm, time= 45 s, ramp= 4 s)
6. Bake out on hotplate (95°C for 90 seconds)
7. Place wafer into mask aligner
8. Align chromium mask

9. Expose:

<i>WEC pressure</i>	1.2 – 1.4 bar
<i>Hard contact time</i>	6 s
<i>Expose</i>	13 s
10. Develop for ~ 45 s in maD-323 developer
11. UVO-cleaner for 5 min to remove HMDS from contact area
12. Dip wafer for short time (~ 30 – 210 s; depends on TOX thickness) in buffered hydrofluoric acid (1:20)
13. Place wafer directly after into evaporator
14. Wait for good vacuum (base pressure $< 10^{-7}$ bar)
15. Argon sputtering:

<i>Program</i>	2
<i>Sputtering time</i>	30-40 s
16. Evaporation of aluminum:

<i>Sample temperature</i>	-25°C
<i>Base pressure</i>	$< 10^{-7}$ mbar
<i>Rate</i>	5-10 $\text{\AA}/\text{s}$
<i>Thickness</i>	100-300 nm
17. Lift-off in warm Acetone
18. Rinse in 2-propanol and dry
19. Anneal in annealing oven AZ500 (MBE Komponenten GmbH):

step	temperature	time	process
1	120	60	4
2	120	600	3
3	120	600	1
4	460	35	4
5	450	600	1

- **ALD protection layer**

1. Dip wafer in buffered hydrofluoric acid (1:20) to remove native oxide (~ 10 s)
2. Wash three times in deionized water
3. Mount sample in ALD chamber (Savannah, CambridgeNanotech), pump
4. Heat up to required process temperature $T_{ALD} = 80 - 225^{\circ}\text{C}$

5. Start program:

step	command	number	time
0	pulse	0	0.05
1	wait	-	12
2	pulse	<i>lor2</i>	0.04
3	wait	-	10
4	goto	0	<i>xtimes</i>

6. Wait until $T = 80^{\circ}\text{C}$

7. Vent chamber, take out sample

● **Microchannel AZ2070**

1. Place wafer onto the spinner
2. Cover wafer with AZ 826 MIF 2070 (AZ electronic materials)
3. Spin film (4000 rpm, time= 40 s, ramp= 4 s)
4. Bake out on hotplate (110°C for 60 seconds)
5. Place wafer into mask aligner
6. Align chromium mask
7. Expose:

<i>WEC pressure</i>	1.2 – 1.4 bar
<i>Hard contact time</i>	5 s
<i>Expose</i>	5 s
8. Postbake on hotplate (110°C for 60 seconds)
9. Develop for ~ 30 s in AZ 826 MIF developer (DEAZ)
10. Resist hardening:
 - a) Post exposure under mask aligner for 30 s
 - b) Slowly heat up to 190°C for 10 min
 - c) Slowly cool down to room temperatur ~ 2 h

● **Microchannel SU-8**

1. Place wafer onto the spinner
2. Cover wafer with SU-8 2002 (Microchem Copr.)
3. Spin film 1. (500 rpm, time= 10 s, ramp= 5 s)
4. Spin 2. (3000 rpm, time= 30 s, ramp= 9 s)
5. Bake out on hotplate (95°C for 60 seconds)

6. Place wafer into mask aligner
7. Align chromium mask
8. Expose:

<i>WEC pressure</i>	1.2 – 1.4 bar
<i>Hard contact time</i>	5 s
<i>Expose</i>	2.5 s
9. Postbake **immediately** on hotplate (95°C for 60 seconds)
10. Develop for ~ 60 s in SU-8 developer (1-methoxy-2-propyl acetate)
11. Clean and dry in 2-propanol
12. Hardbake on hotplate (200°C for 10 min)

- **Bonding**

<i>Model</i>	4523 AD, CMTec
<i>Power</i> ₁	1.44
<i>Time</i> ₁	4
<i>Force</i> ₁	1.4
<i>Power</i> ₂	1.1
<i>Time</i> ₂	4.8
<i>Force</i> ₂	0.7
<i>Tail</i>	1.1
<i>Mode</i>	automatic

- **Epoxy sealing**

1. Mix epoxy EPO-TEK 302-3M (EPOTEK Technologies, mixture A:B - 1:0.45)
2. Place mixture in vacuum chamber
3. Outgas under vacuum for 20 min
4. Slowly seal the sample
5. After ~ 2.5 h close the top of the device, leaving a small opening over the microchannel
6. Harden epoxy for 24 h at room temperature

- **Optional steps**

1. On-chip electrodes
 - a) Place device or wafer onto the spinner
 - b) Cover wafer with ma-N 415

- c) Spin film (4000 rpm, time= 45 s, ramp= 4 s)
 - d) Bake out on hotplate (95°C for 90 seconds)
 - e) Place wafer into mask aligner
 - f) Expose:

<i>Newton rings</i>	broaden and homogeneous distributed
<i>WEC pressure</i>	1.2 – 1.4 bar
<i>Hard contact time</i>	6 s
<i>Expose</i>	13 s
 - g) Develop for ~ 45 s in maD-323 developer
 - h) Evaporation of titanium (adhesion layer):

<i>Sample temperature</i>	23°C
<i>Base pressure</i>	$8 \cdot 10^{-7}$ mbar
<i>Rate</i>	1-2 Å/s
<i>Thickness</i>	5 nm
 - i) Evaporation of platinum or gold:

<i>Sample temperature</i>	23°C
<i>Base pressure</i>	$8 \cdot 10^{-7}$ mbar
<i>Rate</i>	1-2 Å/s
<i>Thickness</i>	100 nm
 - j) Lift-off in warm acetone
 - k) Rinse in 2-propanol and dry
2. Silicon nanowire TOX layer etching
- a) Place device or wafer onto the spinner
 - b) Cover wafer with (HMDS)
 - c) Spin film (4000 rpm, time= 45 s, ramp= 4 s)
 - d) Cover wafer with ma-N 415
 - e) Spin film (4000 rpm, time= 45 s, ramp= 4 s)
 - f) Bake out on hotplate (95°C for 90 seconds)
 - g) Place wafer into mask aligner
 - h) Align chromium mask
 - i) Expose:

<i>WEC pressure</i>	1.2 – 1.4 bar
<i>Hard contact time</i>	6 s
<i>Expose</i>	13 s

- j) Develop for ~ 45 s in maD-323 developer
- k) UVO-cleaner for 5 min to remove (HMDS) from opened area
- l) Dip wafer for short time ($\sim 30 - 210$ s; depends on TOX thickness) in buffered hydrofluoric acid (1:20)
- m) Dissolve maN-415 in Aceton
- n) Rinse in 2-propanol and dry

- **PDMS stamp**

1. Mix PDMS Sylgard 184 (Dow Corning, mixture A:B - 10:1)
2. Place mixture in vacuum chamber
3. Outgas under vacuum for 20 min
4. Pour mixture into mould
5. Bake out in oven (60°C for 3 – 4 hours)

Appendix B: Device fabrication protocol 2

- **Wafer specifications**

Wafer type	8 inch Silicon-On-Insulator (SOI), bonded
Supplier	SOITEC, France
Orientation	(100)
Dopant	p, boron
Resistivity	8.5-11.5 Ωcm
Si device layer thickness	88 nm
Buried SiO ₂ layer thickness	145 nm

- **Thermal oxidation**

Dry oxidation of 1/4 of 8 inch wafer at PSI. Formation of 10-15 nm top SiO₂. Resulting Si device layer thickness 80-85 nm.

- **Alignment marker fabrication**

1. Spin one layer of PMMA 672.11, 1500 rpm ($\sim 3 \mu\text{m}$), marker size $10 \mu\text{m} \times 10 \mu\text{m}$.
2. Write markers, dose = $1000 \mu\text{C}/\text{cm}^2$.
3. Develop for 2 min in IPA:MIBK solution (3:1, Hamatek), rinse in IPA for 30 s
4. Reactive ion etching (RIE) of markers through several wafer layers: 2 min CHF₃ to remove top SiO₂, 5 min CHF₃ and SF₆ (4 sccm) for Si device layer, 8 min CHF₃ for buried SiO₂, 21 min CHF₃ and SF₆ (4 sccm) for Si substrate. Resulting marker depth: $1 \mu\text{m}$.
5. Remove PMMA in acetone.

- **Electron beam lithography of device**

1. Spin HMDS adhesion layer at 4000 rpm. Bake for 1 min at 110°C.
2. Spin nLOF resist (diluted 1:4) at 2500 rpm. Bake for 1 min at 110°C.
3. Expose with dose = $180 \mu\text{C}/\text{cm}^2$.
4. Bake nLOF for 1 min at 110°C.

5. Develop in MIF 826 for 20 - 30 s.
6. Etch most of top oxide by RIE for ~ 30 s (12 sccm CHF_3 and 38 sccm Ar).
7. Remove remaining oxide in buffered HF (4s).
8. Etch Si device layer in TMAH at 45°C for ~ 2 min.
9. Leave sample in n-methyl-2-pyrrolidone (NMP) for several hours at 70°C to remove nLOF residuals.
10. Clean samples by oxygen plasma (5 min, 30 W, 40 sccm O_2 , 200 mTorr).

• **Contact implantation**

1. Spin PMMA 697.04 at 1000 rpm. Spin second layer of PMMA 697.04 at 2000 rpm.
2. Bake samples for more than 1 hour.
3. Cool down samples to $40\text{-}50^\circ\text{C}$ for more than 1 hour.
4. Expose with e-beam to shape mask for implantation: dose $750 \mu\text{C}/\text{cm}^2$.
5. Develop for ~ 3 min.
6. Ship samples to Ion Beam Services (IBS), Peynier, France.
7. Ion implantation at IBS (BF_2^+ , energy = 33 keV, dose = $2.3 \times 10^{15} \text{ cm}^{-2}$)
8. Remove exposed PMMA in acetone overnight at 25°C (at PSI).
9. Clean samples by oxygen plasma (10 min, 30 W, 40 sccm O_2 , 200 mTorr).
10. Thermally anneal samples in forming gas to activate the dopants (at 950°C for 6 min).

• **RCA cleaning of samples and atomic layer deposition (ALD) of gate dielectric**

1. Piranha cleaning ($\text{H}_2\text{O}:\text{H}_2\text{SO}_4$, 2:1) for 10 min at 90°C .
2. Buffered HF for ~ 35 s to remove thermal top oxide.
3. Standard clean 1 ($\text{H}_2\text{O}:\text{H}_2\text{O}_2:\text{NH}_4\text{OH}$, 20:4:1) for 10 min to remove organic contamination.
4. Buffered HF dip for 1 - 2 s.
5. Standard clean 2 ($\text{H}_2\text{O}:\text{H}_2\text{O}_2:\text{HCl}$, 20:1:1) for 10 min at 65°C to remove metallic contamination.
6. ALD of Al_2O_3 at 225°C or HfO_2 at 200°C (200 cycles).

- **Optical lithography for ohmic contacts**

1. Bake at 200°C for 30 min to dehydrate surface.
2. Spin HDMS at 4000 rpm, bake for 1 min at 110°C.
3. Spin diluted resist nLOF:EBR (2:1) at 6000 rpm. Bake for 1 min at 110°C.
4. Place in mask aligner, align and expose for 6 s.
5. Post-bake for 1 min at 110°C.
6. Develop in AZ MIF 826 for 30 – 50 s.
7. Remove oxide from contact pads in buffered HF (1:7, 35 s).
8. Evaporate 300 nm AlSi 1%.
9. Lift-off in NMP.
10. Anneal contact pads in forming gas (10 min at 450°C).
11. Electrical tests.

- **Optical lithography of protective resist (SU-8)**

1. Spin SU-8 2002 at 4000 rpm, bake for 1 min at 110°C
2. Place in mask aligner, align and expose for 18 s.
3. Post-bake for 1 min at 95°C
4. Develop in EC 11 for 90 s (1-methoxy-2-propylacetate).
5. Hard bake at 200°C for 30 min, gradual cool down.

- **Dicing**

1. Spin protective lacquer (S1813) at 2000 rpm. Bake for 1 min 20 s at 110°C.
2. Cut the wafer.
3. Dissolve protective lacquer in acetone (some minutes).

- **Packaging**

1. Wire-bonding in a 64 pins chip carrier (IPK64F1-2219A, NTK Technologies Inc.).
2. Seal contact pads by pouring epoxy (Epotek 353ND, Epoxy Technology) around a PDMS stamp pressed on the sample. Cure in an oven at 120°C for 5 – 10 min.

Appendix C: Protocol for covalent attachment of ionophores

- **Silanization**

4 pieces of about $1 \times 1 \text{ cm}^2$ Al_2O_3 -coated wafers (controls) and a nanowire sample (M18-1) are cleaned with EtOH, wiped with a Kimtech wiper and dried with N_2 . They are then activated with a UV/ozone cleaner for 30 min. The wafer bits and the sample are then placed in a glass Petri dish together with a small watch glass filled with 0.4 ml of (3-Glycidioxypropyl)triethoxysilane (GOPS 3, ABCR153338). The Petri dish is then placed in an oven at 80°C overnight. After 18 h the oven is set to 120°C for 2 h. The silanized surfaces are then flushed with EtOH and dried under a N_2 stream before curing at 80°C for 2.5 h.

Contact angle results measured on controls: 70.8 ± 0.38 (average of 3 measurements against water)

- **Crown ether grafting**

Preparation of solution. A solution of aminomethyl-18-crown-6 (Sigma 388432) in filtered phosphate buffer ($\text{pH} = 8.0$) is prepared by adding $40 \mu\text{l}$ (0.121 mmol/l) of crown ether into $900 \mu\text{l}$ of buffer yielding a 134.4 mM solution. pH was controlled and adjusted to $\text{pH} = 9$ by addition of $10 \mu\text{l}$ of 37% HCl .

Procedure for control samples. 2 pieces of previously silanized Al_2O_3 wafer (controls) are placed in a petri dish and covered with $\sim 250 \mu\text{l}$ of the previously prepared solution, and a wet pad (paper saturated with water) is added to the dish to prevent evaporation of the solution by saturating the atmosphere. After 22 h, the bits are dipped into ultrapure water and then washed with 10 ml of ultrapure water and then 10 ml of EtOH. They are dried under a N_2 stream.

Contact angles are measured on controls: 55.4 ± 2.23 (average of 3 measurements against water)

Procedure for nanowire samples. The sample is mounted together with the PDMS fluidics and the small metallic plate into the press and

equipped with teflon tubes (2 inlets and 2 outlets to separately access different sample parts). A 1 ml syringe mounted on a syringe-pump, filled with 300 μ l of the previously prepared solution is connected to the inlet. The fluidics are first filled manually, and then flown by the pump overnight (flow of 0.01 ml/h). After 15 h the flow is risen to 0.02 ml/h for 6 h. The syringe is then removed and the fluidics are flushed manually with 6 ml of ultra pure water and then 6 ml of EtOH. It is the dried with a N₂ stream through the teflon tubings and fluidics. The fluidics are then dismantled and the surface refushed with \sim 6 ml of EtOH and dried with a N₂ stream.

Appendix D: Surface modification protocol for lectin detection

- **Silanization.** The samples are activated by UV/ozone treatment for 30 min. Then, a droplet of pure Aminopropyldimethylmethoxysilane (APTES 1) is placed together with the sample in an oven at 80°C (overnight), followed by curing at 80°C for 1 hour.
- **Preparation of solutions for linker attachment.** Sulfo-NHS (N-hydroxysulfosuccinimide, 10 equivalents) and EDC (1-ethyl-3-(3-dimethylaminopropyl) carbodiimide, 5 equivalents) are dissolved in phosphate buffer (5 mM, pH 6) and stirred until complete dissolution (pH at this point nearly 5), then the sugar (n-heptyl-mannose) amount needed (in bidistilled water) is added to a final volume of 0.5 ml. The mixture is stirred for 25 min at 25°C. The solution is then diluted in phosphate buffer (100 mM, pH 8), and the pH adjusted to 7.5 with NaOH (0.35 ml, if needed). The solution is then diluted to the volume needed to have a 6 mM concentration relative to the sugar, with the same buffer. A solution of 8-OH heptanoic acid sulfo-NHS ester was prepared the same way (negative control).
- **Surface functionalization of the nanowire chip.** The sample is mounted together with the PDMS fluidics and the small metallic plate into the press and equipped with teflon tubes (2 inlets and 2 outlets to separately functionalize different sample parts). The previously prepared solutions are pumped through the channels by an automatic syringe pump (250 μ l syringe, 0.05 mm/min, 13 h). The fluidics is then unmounted and the sample is washed with deionized water.

Publication List

Peer-reviewed journal publications

1. S. Hugger, H. Xu, A. Tarasov, M. Cerchez, T. Heinzl, I. V. Zozoulenko, D. Reuter, and A. D. Wieck. Magnetic-barrier-induced conductance fluctuations in quantum wires. *Phys Rev. B* **78**, 165307 (2008)
2. A. Tarasov, S. Hugger, H. Xu, M. Cerchez, T. Heinzl, I. Zozoulenko, U. Gasser-Szerer, D. Reuter, and A. D. Wieck. Quantized magnetic confinement in quantum wires. *Phys Rev. Lett.* **104**, 186801 (2010)
3. O. Knopfmacher, A. Tarasov, W. Fu, M. Wipf, B. Niesen, M. Calame, and C. Schönenberger. Nernst Limit in Dual-Gated Si-Nanowire FET Sensors. *Nano Lett.* **10**, 2268-2274 (2010)
4. A. Tarasov, W. Fu, O. Knopfmacher, J. Brunner, M. Calame, and C. Schönenberger. Signal-To-Noise Ratio in Dual-Gated Silicon Nanoribbon FET Sensors. *Appl. Phys. Lett.* **98**, 012114 (2011)
5. W. Fu, C. Nef, O. Knopfmacher, A. Tarasov, M. Weiss, M. Calame, and C. Schönenberger. Graphene Transistors Are Insensitive to pH Changes in Solution. *Nano Lett.* **11**, 3597-3600 (2011)
6. O. Knopfmacher, A. Tarasov, M. Wipf, W. Fu, M. Calame, and C. Schönenberger. Silicon-Based Ion-Sensitive Field-Effect Transistor Shows Negligible Dependence on Salt Concentration at Constant pH. *ChemPhysChem* **13**, 1157-1160 (2012)
7. A. Tarasov, M. Wipf, K. Bedner, J. Kurz, W. Fu, V. A. Guzenko, O. Knopfmacher, R. L. Stoop, M. Calame, and C. Schönenberger. True Reference Electrode Realized with Silicon Nanowires. *Langmuir* **28**, 9899-9905 (2012)
8. A. Tarasov, M. Wipf, R. L. Stoop, K. Bedner, W. Fu, V. A. Guzenko, O. Knopfmacher, M. Calame, and C. Schönenberger. Understanding the Electrolyte Background for Biochemical Sensing with Ion-Sensitive Field-Effect Transistors, *ACS Nano* **6**, 9291-9298 (2012)

9. M. Wipf, A. Tarasov, R. L. Stoop, K. Bedner, W. Fu, J. Kurz, J. Grognux, I. Wright, M. Calame, and C. Schönenberger. Differential Detection of Alkaline Ions Using Multifunctional Silicon Nanowire Arrays, *in preparation*.
10. W. Fu, C. Nef, A. Tarasov, M. Wipf, R. Stoop, M. Weiss, M. Calame, and C. Schönenberger. Ion-Sensitive Graphene Field-Effect Transistors Enabled by Noncovalent Functionalization, *in preparation*
11. K. Bedner, V. A. Guzenko, A. Tarasov, M. Wipf, R. L. Stoop, J. Brunner, W. Fu, R. A. Minamisawa, C. David, M. Calame, J. Gobrecht, and C. Schönenberger. Scaling of Noise Limitations in Silicon Nanowire Charge Sensors, *in preparation*

International conferences

- A. Tarasov, S. Hugger, M. Cerchez, H. Xu, T. Heinzl. Transport Through Magnetic Barriers in 2DEGs and Quantum Wires. *Nanoelectronics Days*, Aachen, Germany, May 13-16, 2008 (talk).
- A. Tarasov, O. Knopfmacher, W. Fu, M. Calame, and C. Schönenberger. Nernst Limit in Dual-Gated FET Sensors. *Annual Meeting of the Swiss Physical Society*, Basel, Switzerland, June 21-22, 2010 (talk).
- A. Tarasov, O. Knopfmacher, W. Fu, M. Calame, and C. Schönenberger. Sensing with Dual-Gated Si Nanowire FETs. *36th International Conference on Micro & Nano Engineering*, Genoa, Italy, September 19-22, 2010 (talk).
- A. Tarasov, O. Knopfmacher, K. Bedner, M. Wipf, W. Fu, M. Calame, and C. Schönenberger. Sensing with Dual-Gated Silicon Nanowire Field-Effect Transistors. *Euroensors XXV*, Athens, Greece, September 4-7, 2011 (talk).
- A. Tarasov, M. Wipf, W. Fu, O. Knopfmacher, J. Kurz, K. Bedner, V. A. Guzenko, A. Odedra, R. L. Stoop, M. Calame, and C. Schönenberger. Detection Limits of Silicon Nanowire Field-Effect Transistors. *Biosensors 2012*, Cancun, Mexico, May 15-18, 2012 (talk).
- A. Tarasov, M. Wipf, W. Fu, O. Knopfmacher, J. Kurz, K. Bedner, V. A. Guzenko, A. Odedra, R. L. Stoop, M. Calame, and C. Schönenberger. Detection Limits of Silicon Nanowire Field-Effect Transistors. *Swiss NanoConvention 2012*, Lausanne, Switzerland, May 22-24, 2012 (poster).

Curriculum Vitae

Personal Information

Surname: Tarasov
Given Name: Alexey
Date of Birth: September 8, 1984
Place of Birth: Novosibirsk, USSR
Nationality: Russian and German
Marital Status: Single

Education

- 06/2009 – 10/2012
University of Basel, PhD in Experimental Physics under the supervision of Prof. Dr. C. Schönberger: “Silicon nanowire field-effect transistors for sensing applications”
- 09/2003 – 04/2009
Heinrich Heine University Düsseldorf, Germany, Diploma in Physics
Diploma thesis under the supervision of Prof. Dr. T. Heinzel: “Transport through magnetic barriers in quantum wires”
- 07/2007 – 12/2007
Macquarie University, Sydney, Australia, Study Abroad
- 08/1999 – 06/2003
Freiherr-vom-Stein Gymnasium (academic high school) Leverkusen, Germany, Abitur
- 09/1990 – 05/1999
Secondary School Nr. 174, Novosibirsk, Russia

Professional Experience

- 06/2009 – present
University of Basel, Department of Physics, Research and Teaching Assistant

- 08/2006 – 09/2006 Procter & Gamble, Schwalbach am Taunus, Germany, Research & Development, Intern
- 09/2005 – 03/2009
Heinrich Heine University Düsseldorf, Undergraduate Teaching Assistant

Voluntary Activities

- 2007 – 2009
Heinrich Heine University Düsseldorf, Germany, Physics Student Representative
- 2005 – 2007
Heinrich Heine University Düsseldorf, Germany, Student Representative in the Physics Department Management

Fellowship

- 03/2005 – 04/2009
Scholarship of the Friedrich Naumann Foundation

Acknowledgements

During my time here in Basel, I have grown a lot as a scientist and as a person. Now it is time to thank all the people who made my stay here unforgettable. First of all, I would like to thank my supervisor Christian Schönenberger for teaching me many things about science and for being a great boss. I will never forget your comment during my first talk on nanowire sensors: “You have to sell it!!!” The meetings with you have been tough sometimes, but always helpful and motivating. You have an excellent feeling for science and for people. Second, I am indebted to Michel Calame for his time, all the countless meetings and discussions that paved the way to a successful thesis. It has been a pleasure working with you!

I am grateful to Prof. Dr. Nico de Rooij and Prof. Dr. Jan Linnros for being co-referees of my thesis.

This thesis has become a success story also because of the great teamwork. I thank the NanowireSensor team for being absolutely determined, hard-working, hard partying, success-oriented, efficient, extremely productive – and for being awesome together. In particular, I give thanks to Oren “Orenic” Knopfmacher aka Dr. O for introducing me to the project and for the amazing collaboration I have enjoyed during the past years. We have shaped the project together and made it a full success, worth many “good results cognacs”. I owe many thanks to Mathias “the rock star” Wipf aka This for being a great colleague and for his tireless quest for the perfect experiment. The project took a big step forward with the countless productive hours we spent side by side. It has been fun working with you! This, I am sure that you will keep up the spirit of the Prolo Team. I am also grateful to Wangyang Fu for the numerous discussions that helped me a lot in understanding things. Ralph “the Anker man” Stoop has joined the project during its most productive phase (so far). With you, Ralph, we have found the missing jigsaw puzzle piece for a perfect team.

I owe thanks to the rest of the room temperature office for a unique atmosphere: Jan “F3K” Brunner for illuminating discussions, M-Budget chewing gums, and for helping me to expand my knowledge of: model sailplanes, climbing, ski bindings, the bitter fate of being an ex-Miss Switzerland and almost everything else. It’s been a pleasure sitting in front of you. Many thanks go to loud, louder, Cornelia Nef for teaching me the culture and the

dialect of the Appenzellerland. It is impossible not to listen to you! I also thank Jón Ágústsson for being a quiet office mate and a not so quiet pal outside :) And I thank Toni Fröhlich for being himself.

A very special thanks goes to Jens “Skindally” Schindele for his friendship, for the “Summer of Glory” 2010 and everything else :) I hope we keep in touch!

Further, I would like to mention the rest of the group (in random order): Hagen Aurich, Matthias Bräuninger, Frank Freitag, Julia Samm, Jelena Trbovic, Roman Huber, Zheng-Ming Wu, Alex Eichler, Haichao Huang, Claire Barrett, Szabolcs Csonka, Gergő Fülöp, Lukas Hofstetter, Andreas Kleine, Songmei Wu, Peter Rickhaus, Jörg Gramich, Thomas Hasler, David Just, Stefan Nau, Gábor Fábrián, Samuel d’Hollosy, Romain Maurand, Andreas Baumgartner, Markus Weiss, Veronica Savu. Thank you all! We had so much fun together!

This project has been a part of the Swiss Nano-Tera network, and I had the pleasure to collaborate with many scientists from all over Switzerland to whom I feel indebted. Especially, I would like to thank Kristine Bedner and Vitaliy Guzenko for providing us with many thousands of nice nanowires. You guys did an amazing job! Jolanta Kurz for teaching me the magic of surface chemistry, and for the functionalization of so many samples. Johann Grognum for successfully taking over this job. Giulio Navarra, Meike Scharenberg, Arjan Odedra, Florian Binder and Beat Ernst for linkers, lectins and discussions. Bernd Dielacher and Janos Vörös for their support with optical measurements and valuable discussions. Sara Rigante for the oxide characterization and for her smart ideas. Paolo Livi for the nice read-out chip. And Matthias Streiff for challenging questions and interesting discussions.

I gratefully acknowledge the excellent work done for our project by the technical staff at the Department of Physics. In particular, I thank Heinz Breitenstein, Silvester Jakob, Sascha Martin and his team, Michael Steinacher, and Andreas Tonin. I also thank Barbara Kammermann and Astrid Kalt for administrative support.

Many thanks go to my family for always supporting me and believing in me. And finally, I thank Franzi for reminding me every day of what *really* matters.